

Phenomenology of a flavored multiscalar Branco-Grimus-Lavoura-like model with three generations of massive neutrinos

P. M. Ferreira,^{1,2,*} Felipe F. Freitas,^{3,†} João Gonçalves^{3,‡}, Antonio P. Morais^{3,§},
Roman Pasechnik^{4,||} and Vasileios Vatellis^{3,¶}

¹*Instituto Superior de Engenharia de Lisboa—ISEL, 1959-007 Lisboa, Portugal*

²*Centro de Física Teórica e Computacional, Faculdade de Ciências, Universidade de Lisboa, Campo Grande, 1749-016 Lisboa, Portugal*

³*Departamento de Física, Universidade de Aveiro and CIDMA, Campus de Santiago, 3810-183 Aveiro, Portugal*

⁴*Department of Astronomy and Theoretical Physics, Lund University, SE-223 62 Lund, Sweden*



(Received 27 April 2022; accepted 29 September 2022; published 17 October 2022)

In this paper, we present several possible anomaly free implementations of the Branco-Grimus-Lavoura (BGL) model with two Higgs doublets and one singlet scalar. The model also includes three generations of massive neutrinos that get their mass via a type-I seesaw mechanism. A particular anomaly free realization, which we dub ν BGL-1 scenario, is subjected to an extensive phenomenological analysis, from the perspective of flavor physics and collider phenomenology.

DOI: [10.1103/PhysRevD.106.075017](https://doi.org/10.1103/PhysRevD.106.075017)

I. INTRODUCTION

With the discovery of the Higgs boson at the LHC in 2012 [1,2], the entire particle spectrum of the Standard Model (SM) has been observed and experimentally validated. However, despite its remarkable success, there is experimental evidence for the existence of Dark Matter (DM) and neutrino masses, while the observed hierarchical structure that characterizes the fermion sector finds no explanation in the SM. With a plethora of New Physics (NP) extensions that aim at offering solutions to the aforementioned phenomena, the vast majority of them come in the form of extended scalar sectors. One of the most popular and thoroughly explored multiscalar scenarios is the two-Higgs doublet model (THDM), as first proposed by T.D. Lee [3]. The introduction of a new complex scalar doublet, in addition to the one that is already present in the SM, results in an extended particle spectrum with a new electrically charged scalar and two new neutral ones, one of

which is even while the other is odd under discrete CP (charge times parity) transformations.

This type of model provides a rich breeding ground for phenomenological studies, with the possibility of having a suitable DM candidate in its spectrum [4–9], spontaneous CP -violation [10–14], and generation of flavor-changing neutral currents (FCNCs) mediated by the new neutral scalars [15,16]. However, the presence of FCNCs can be troublesome since they are very constrained experimentally, and in the models we are discussing they can manifest themselves already at tree-level, whereas equivalent processes in the SM are of pure radiative origin, thus highly suppressed. As such, one either requires FCNCs couplings to be fine-tuned or rather there should exist an underlying symmetry that naturally mitigates the effect of these interactions. A concrete mechanism for symmetry-suppressed FCNCs has been proposed by Branco, Grimus, and Lavoura [17] where, due to the presence of an Abelian flavor symmetry such as \mathbb{Z}_2 or $U(1)$, FCNC couplings are kept under control by making such interactions proportional to off-diagonal elements of the Cabibbo-Kobayashi-Maskawa (CKM) matrix. Such a class of models is commonly dubbed as Branco-Grimus-Lavoura (BGL) models.

A natural extension of the THDM-BGL framework can emerge in the form of a gauge $U(1)$ symmetry, which necessarily requires a further enlargement of the scalar sector with a new electroweak (EW) singlet, thus falling in the family of next-to-minimal THDM (or NTHDM) for short. Recently, a complete list of all possible anomaly free implementations of the gauged NTHDM with two families

*pedro.ferreira@fc.ul.pt

†felipefreitas@ua.pt

‡jpedropino@ua.pt

§aapmorais@ua.pt

||Roman.Pasechnik@thep.lu.se

¶vasileios.vatellis@gmail.com

Published by the American Physical Society under the terms of the [Creative Commons Attribution 4.0 International license](https://creativecommons.org/licenses/by/4.0/). Further distribution of this work must maintain attribution to the author(s) and the published article's title, journal citation, and DOI. Funded by SCOAP³.

of right-handed neutrinos and a type-I seesaw mechanism was introduced in Ref. [18], while a generalization to three neutrino generations was discussed in Ref. [19]. For previous phenomenological considerations in a set of THDMs featuring the absence of tree-level FCNCs and accommodating a seesaw mechanism for neutrino mass generation, see Ref. [20]. Among all allowed textures in the Yukawa sector one of them replicates the BGL structure. The model explored in this article is inspired by such a scenario but for the case of a global $U(1)'$ flavor symmetry. The latter is explicitly broken via soft terms in the scalar potential as well as by the vacuum expectation value (VEV) in the real component of the complex singlet scalar field. As a result, in addition to a SM-like Higgs boson candidate, five new physical scalars emerge, including an electrically charged one, H^\pm , two CP -even neutral ones, H_2 and H_3 , and two pseudoscalars, A_2 and A_3 . Note that in the context of the gauge $U(1)'$ flavor symmetry [18,19] one of those pseudoscalars, as a pure Goldstone particle, becomes a longitudinal polarization mode of a Z' vector boson. In turn, tight constraints imposed by direct searches at the LHC [21–26] on new gauge bosons imply a rather large $U(1)'$ breaking scale, of at least a few TeV, naturally inducing masses of the same order to the new scalars, unless a certain degree of fine-tuning is in place. Our current goal is to study the impact of the extended scalar sectors not too far from the EW scale. For this purpose, a global version of the BGL scenario instead of the gauged one proposed in Ref. [18,19] is considered in this work.

We test the viability of the scalar sector against phenomenological observables, in particular, by making sure that FCNCs obey current experimental constraints and that there exists one CP -even neutral scalar that replicates the properties of the SM Higgs boson, defined as H_1 in this article. For a rigorous analysis we employ widely used open-source software, namely, SARAH [27], for model implementation, and SPheno [28], to numerically calculate masses and interaction vertices, which are then used to interface with HiggsBounds and HiggsSignals [29,30], where the viability of the Higgs sector is verified, and FLAVIO [31], where flavor observables are calculated.

The paper is organized as follows. In Sec. II we introduce the model, with the focus on the Yukawa and scalar sectors of the theory that obey the BGL structure. In Sec. III we detail the method by which one can obtain anomaly free models, as first discussed in Ref. [19], highlighting the possible textures in the lepton sector. In Sec. III E we show all possible anomaly free implementations of the considered class of NTHDM scenarios. In Sec. IV we discuss the particular version of the model considered in this article, with a discussion on the neutrino masses and mixings. In Sec. V we describe the methodology behind the phenomenological studies and present the numerical results that follow. In Sec. VI we confront our results with direct scalar

searches at the LHC. In Sec. VII we conclude with a summary of our findings.

II. A GENERIC NTHDM WITH A BGL STRUCTURE

In this work, we extend the SM with a flavor nonuniversal $U(1)'$ global symmetry alongside three generations of right-handed neutrinos $\nu_R^{1,2,3}$, a scalar singlet S and a second Higgs doublet¹ Φ_2 . In addition, we demand that the singlet and at least one of the doublets transform non-trivially under $U(1)'$ such that at least two VEVs contribute to the breaking of the flavor symmetry.

The Yukawa interactions that define the model to be discussed read as

$$-\mathcal{L}_{\text{Yukawa}} = \overline{q}_L^0 \Gamma_a \Phi^a d_R^0 + \overline{q}_L^0 \Delta_a \tilde{\Phi}^a u_R^0 + \overline{\ell}_L^0 \Pi_a \Phi^a e_R^0 + \overline{\ell}_L^0 \Sigma_a \tilde{\Phi}^a \nu_R^0 + \frac{1}{2} \overline{\nu}_R^{c0} (A + BS + CS^*) \nu_R^0 + \text{H.c.}, \quad (2.1)$$

where Γ , Δ , Π , and Σ are the 3×3 Dirac-like down quark, up quark, charged lepton, and neutrino Yukawa coupling matrices, respectively. The index a runs over the two scalar doublets (with implicit summation) and, as usual, $\tilde{\Phi} \equiv i\sigma_2 \Phi^*$. While B and C are the Majorana-like Yukawa matrices involving right-handed neutrinos and the scalar singlet, A is a Majorana mass term written in the flavor basis, defined by the fields expressed with the 0 superscript. To comply with a BGL structure the transformation laws of the different fields under the $U(1)'$ global symmetry are chosen so that the quark Yukawa textures are given as

$$\Gamma_1: \begin{pmatrix} \times & \times & \times \\ \times & \times & \times \\ 0 & 0 & 0 \end{pmatrix}, \quad \Gamma_2: \begin{pmatrix} 0 & 0 & 0 \\ 0 & 0 & 0 \\ \times & \times & \times \end{pmatrix}, \\ \Delta_1: \begin{pmatrix} \times & \times & 0 \\ \times & \times & 0 \\ 0 & 0 & 0 \end{pmatrix}, \quad \Delta_2: \begin{pmatrix} 0 & 0 & 0 \\ 0 & 0 & 0 \\ 0 & 0 & \times \end{pmatrix}. \quad (2.2)$$

Note that this choice of textures implies that tree-level FCNCs will appear only in the down quark sector, since the up-quark Yukawa matrices can be diagonalized simultaneously. Indeed, this represents the more conservative scenario, since down-type FCNCs are more tightly constrained by experiment when compared to those in the up-sector. Of course, one can also extend the BGL mechanism to the lepton sector, as first proposed in Ref. [33], which is beyond the scope of the present work.

¹The BGL model versions discussed in this article were first introduced in the Appendix of [32].

In Eq. (2.1), the scalar fields can be expanded as

$$\begin{aligned}\Phi_a &\equiv \frac{1}{\sqrt{2}} \begin{pmatrix} \sqrt{2}\phi_a^+ \\ v_a e^{i\varphi_a} + R_a + iI_a \end{pmatrix}, \\ S &\equiv \frac{1}{\sqrt{2}} (v_S e^{i\varphi_S} + \rho + i\eta),\end{aligned}\quad (2.3)$$

where $v_{1,2}$ and v_S denote the doublet and singlet VEVs, respectively. As the scalar fields have, in general, different $U(2)_Y \times U(1)'$ charge assignment, we can choose two of the VEVs real, for example v_1 and v_2 , i.e. $\varphi_{1,2} = 0$. In multi-Higgs SM extensions there is a possibility to trigger spontaneous CP breaking via complex VEVs. For the purposes of this work, however, we are only focused on a CP conserving scalar phase. CP violation will emerge via the CKM matrix as in the SM, due to the fact that the entries of the Yukawa matrices of Eq. (2.2) are complex.

Once the two doublets acquire VEVs, both the quarks and the charged leptons obtain tree-level masses which are given by

$$\begin{aligned}M_u^0 &\equiv \frac{1}{\sqrt{2}} (v_1 \Delta_1 + v_2 \Delta_2), \\ M_d^0 &= \frac{1}{\sqrt{2}} (v_1 \Gamma_1 + v_2 \Gamma_2), \\ M_e^0 &= \frac{1}{\sqrt{2}} (v_1 \Pi_1 + v_2 \Pi_2).\end{aligned}\quad (2.4)$$

One can rotate the spectrum to the mass basis via biunitary transformations of the form

$$D_f = U_{fL}^\dagger M_f^0 U_{fR},\quad (2.5)$$

with D_f a diagonal mass form with ordered fermion masses and where $U_{fL,R}$ are unitary matrices with the subscript f indicating the fermion flavor, i.e. $f = e, u, d$. Following the standard notation, one can define the following matrices:

$$N_u^0 = \frac{1}{\sqrt{2}} (v_2 \Delta_1 - v_1 \Delta_2) \quad N_d^0 = \frac{1}{\sqrt{2}} (v_2 \Gamma_1 - v_1 \Gamma_2),\quad (2.6)$$

whose off-diagonal elements are responsible for inducing tree-level FCNC interactions. The key feature of the BGL model is that such matrices can be reexpressed solely in terms of quark masses, CKM mixing elements $V_{ij} \equiv \sum_k (U_{uL})_{ik} (U_{dL}^\dagger)_{kj}$, with $i, j, k = 1, 2, 3$, and the ratio $t_\beta \equiv \tan \beta \equiv v_1/v_2$ as follows:

$$\begin{aligned}(N_u)_{ij} &= (t_\beta \delta_{ij} - (t_\beta + t_\beta^{-1}) \delta_{ij} \delta_{j3}) m_{u_j}, \\ (N_d)_{ij} &= (t_\beta \delta_{ij} - (t_\beta + t_\beta^{-1}) V_{3i}^* V_{3j}) m_{d_j},\end{aligned}\quad (2.7)$$

such that the down-specific FCNCs are controlled by the smallness of the off-diagonal CKM mixing elements V_{3i} .

For the charged lepton sector, the generic coupling combinations can be found in complete analogy with the quarks, i.e.

$$M_e^0 = \frac{1}{\sqrt{2}} (v_1 \Pi_1 + v_2 \Pi_2), \quad N_e^0 = \frac{1}{\sqrt{2}} (v_2 \Pi_1 - v_1 \Pi_2).\quad (2.8)$$

Last but not least, the neutrino sector is equipped with a seesaw mechanism of type-I, as soon as the singlet S develops a VEV. In particular, defining

$$n_L^0 \equiv \begin{pmatrix} \nu_L^0 \\ \nu_R^c \end{pmatrix},\quad (2.9)$$

one can recast the neutrino mass Lagrangian as

$$-\mathcal{L}_\nu^{\text{mass}} = \frac{1}{2} \overline{n_L^0} \mathcal{M} n_L^{0,c} + \text{H.c.},\quad (2.10)$$

where

$$\mathcal{M} \equiv \begin{pmatrix} 0 & m_D \\ m_D^T & M_R \end{pmatrix},\quad (2.11)$$

and with the Dirac and Majorana neutrino masses given by

$$\begin{aligned}m_D &\equiv \frac{1}{\sqrt{2}} (v_1 \Sigma_1 + v_2 \Sigma_2), \\ M_R &\equiv A + \frac{v_S}{\sqrt{2}} (B + C),\end{aligned}\quad (2.12)$$

respectively. Here, we have also considered that the singlet VEV is real. At low energies, in the limit of $M_R \gg m_D/m_D^T$, the effective Lagrangian for the light active neutrinos takes the form

$$-\mathcal{L}_\nu^{\text{eff}} \equiv \frac{1}{2} \overline{\nu_L^0} m_\nu \nu_L^{0,c} + \text{H.c.},\quad (2.13)$$

with

$$m_\nu \equiv -m_D M_R^{-1} m_D^T.\quad (2.14)$$

The numerical analysis performed in this study relies on an inversion procedure analogous to that developed in [34]. In particular, for the quark sector, one uses their physical masses as well as the CKM mixing elements as input parameters. However, due to a rich neutrino content, one cannot analytically invert the entire lepton sector. Instead, while electron, muon and tau masses are given as input parameters, one performs a numerical fit to neutrino masses alongside an extended version of the Pontecorvo-Maki-Nakagawa-Sakata (PMNS) matrix, as it is discussed in Sec. IV.

The most generic form of the scalar potential can be written as

$$V = V_0 + V_1 \quad (2.15)$$

with

$$\begin{aligned} V_0 &= \mu_i^2 |\Phi^i|^2 + \lambda_i |\Phi^i|^4 + \lambda_3 |\Phi_1|^2 |\Phi_2|^2 + \lambda_4 |\Phi_1^\dagger \Phi_2|^2 \\ &\quad + \mu_S^2 |S|^2 + \lambda'_1 |S|^4 + \lambda'_2 |\Phi_1|^2 |S|^2 + \lambda'_3 |\Phi_2|^2 |S|^2 \quad \text{and} \\ V_1 &= \mu_3^2 \Phi_2^\dagger \Phi_1 + \frac{1}{2} \mu_b^2 S^2 + a_1 \Phi_1^\dagger \Phi_2 S + a_2 \Phi_1^\dagger \Phi_2 S^\dagger \\ &\quad + a_3 \Phi_1^\dagger \Phi_2 S^2 + a_4 \Phi_1^\dagger \Phi_2 S^{\dagger 2} + \text{H.c.} \end{aligned} \quad (2.16)$$

While in V_0 we adopt the usual notation where $\mu_{i,S}$ represents quadratic mass parameters and λ_i, λ'_i are the quartic couplings, in V_1 $a_{1,2}$ denote cubic couplings between the Higgs doublets and the singlet while $a_{3,4}$ are the quartic couplings between the two Higgs doublets and the scalar singlet field. Given that the singlet S carries a nontrivial $U(1)'$ charge X_S , then, out of the four $a_{1,2,3,4}$ terms, only one is allowed in the limit of an exact $U(1)'$. However, both a_1 and a_2 , as well as μ_b^2 , can be introduced to softly break the flavor symmetry and are allowed to coexist with either a_3 or a_4 [18,19].

III. ANOMALY FREE BGL IMPLEMENTATION

The transformation properties of the quark and scalar fields under the $U(1)'$ flavor symmetry are given, as usual, by

$$\Psi_i \rightarrow e^{i\theta X_{\Psi_i}} \Psi_i, \quad (3.1)$$

where $\Psi_i \in (q_L^0, u_R^0, d_R^0, \Phi_1, \Phi_2, S)$, and where X_{Ψ_i} are the corresponding $U(1)'$ charges with θ a global phase parameter. It then follows that the Yukawa matrices transform as

$$\begin{aligned} (\Gamma_a)_{ij} &= e^{i\theta(X_{q_i} - X_{d_j} - X_{\Phi_a})} (\Gamma_a)_{ij}, \\ (\Delta_a)_{ij} &= e^{i\theta(X_{q_i} - X_{u_j} + X_{\Phi_a})} (\Delta_a)_{ij}, \end{aligned} \quad (3.2)$$

such that textures on $(\Gamma_a)_{ij}$ result from a set of linear constraints that read as

$$\begin{aligned} (\Gamma_a)_{ij} &= \text{any if } X_{q_i} - X_{d_j} = X_{\Phi_a}, \\ (\Gamma_a)_{ij} &= 0 \quad \text{if } X_{q_i} - X_{d_j} \neq X_{\Phi_a}. \end{aligned} \quad (3.3)$$

The same can be done in the up-quark sector by trading $(\Gamma_a)_{ij} \rightarrow (\Delta_a)_{ij}$, $X_{d_j} \rightarrow X_{u_j}$, and $X_{\Phi_a} \rightarrow -X_{\Phi_a}$. Among many possible solutions found in Refs. [19] and [18], the

well-known quark BGL textures [see Eq. (2.2)], that are used in this work, satisfy the following 36 constraints:

$$\begin{aligned} X_{q_{1,2}} - X_{d_{1,2,3}} &= X_{\Phi_1}, & X_{q_3} - X_{d_{1,2,3}} &\neq X_{\Phi_1}, \\ X_{q_3} - X_{d_{1,2,3}} &= X_{\Phi_2}, & X_{q_{1,2}} - X_{d_{1,2,3}} &\neq X_{\Phi_2}, \\ X_{q_{1,2}} - X_{u_{1,2}} &= -X_{\Phi_1}, & X_{q_3} - X_{u_{1,2,3}} &\neq -X_{\Phi_1}, \\ X_{q_{1,2}} - X_{u_3} &\neq -X_{\Phi_1}, & X_{q_3} - X_{u_3} &= -X_{\Phi_2}, \\ X_{q_{1,2}} - X_{u_{1,2,3}} &\neq -X_{\Phi_2}, & X_{q_3} - X_{u_{1,2}} &\neq -X_{\Phi_2}. \end{aligned} \quad (3.4)$$

Focusing now on the lepton and neutrino sectors, one must consider all possible textures of the Dirac-like Π_a and Σ_a and Majorana-like B and C Yukawa matrices, as well as on the A mass matrix. To do so one considers that

- (i) there are no massless charged leptons yielding $\det M_e \neq 0$;
- (ii) there are three generations of massive neutrinos such that² $\det M_\nu \neq 0$;
- (iii) there is a nonzero complex phase in the PMNS matrix which implies that $\det[M_e M_e^\dagger] \neq 0$ and $\det[M_\nu M_\nu^\dagger] \neq 0$.

Notice that the second condition is the only one differing from those first introduced in Ref. [19] and [18]. For a type-I seesaw mechanism such a condition also translates into M_R and M_D being 3×3 matrices with nonzero determinant. Note also that any two models that can be mapped from one another via a permutation are equivalent as it would simply correspond to a relabeling of flavor indices. Defining the new primed Yukawa and mass matrices as

$$\begin{aligned} \Gamma'_{1,2} &= \mathcal{P}_i^\dagger \Gamma_{1,2} \mathcal{P}_j, & \Delta'_{1,2} &= \mathcal{P}_i^\dagger \Delta_{1,2} \mathcal{P}_k, \\ \Pi'_{1,2} &= \mathcal{P}_i^\dagger \Pi_{1,2} \mathcal{P}_m, & \Sigma'_{1,2} &= \mathcal{P}_i^\dagger \Sigma_{1,2} \mathcal{P}_n, \\ A' &= \mathcal{P}_n^\dagger A \mathcal{P}_n, & B' &= \mathcal{P}_n^\dagger B \mathcal{P}_n, & C' &= \mathcal{P}_n^\dagger C \mathcal{P}_n, \end{aligned} \quad (3.5)$$

with \mathcal{P} being a three-dimensional representation of the permutation group S_3 , with all indices running from one to six, one excludes all such additional textures that can be obtained by permutations in the flavor space.

A. Majorana neutrino sector

In total, there are 11 minimal textures for A , B , and C that fulfil the constraint of M_R being a 3×3 symmetric matrix with a nonzero determinant. These are

²Note that there exists no anomaly free implementation of the BGL textures with two generations of massive neutrinos, as shown in Ref. [18].

$$\begin{aligned}
(1) \quad & A: \begin{pmatrix} \times & 0 & 0 \\ 0 & 0 & \times \\ 0 & \times & 0 \end{pmatrix}, & B: \mathbf{0}, & C: \mathbf{0}, \\
(2) \quad & A: \begin{pmatrix} \times & 0 & 0 \\ 0 & 0 & 0 \\ 0 & 0 & 0 \end{pmatrix}, & B: \begin{pmatrix} 0 & 0 & 0 \\ 0 & 0 & \times \\ 0 & \times & 0 \end{pmatrix}, & C: \mathbf{0}, \\
(3) \quad & A: \begin{pmatrix} \times & 0 & 0 \\ 0 & 0 & 0 \\ 0 & 0 & 0 \end{pmatrix}, & B: \begin{pmatrix} 0 & 0 & 0 \\ 0 & \times & 0 \\ 0 & 0 & 0 \end{pmatrix}, & C: \begin{pmatrix} 0 & 0 & 0 \\ 0 & 0 & 0 \\ 0 & 0 & \times \end{pmatrix}, \\
(4) \quad & A: \begin{pmatrix} 0 & \times & 0 \\ \times & 0 & 0 \\ 0 & 0 & 0 \end{pmatrix}, & B: \begin{pmatrix} 0 & 0 & \times \\ 0 & 0 & 0 \\ \times & 0 & 0 \end{pmatrix}, & C: \begin{pmatrix} 0 & 0 & 0 \\ 0 & 0 & \times \\ 0 & \times & 0 \end{pmatrix},
\end{aligned} \tag{3.6}$$

where textures (1) and (2) come in three and six versions, respectively, taking into account all possible permutations of A , B , and C . For textures (3) and (4), on the other hand, we only need to consider those shown above as permutations of rows and columns solely correspond to a relabeling of flavor indices. In the presence of the $U(1)'$ flavor symmetry one must also consider the transformation laws

$$\begin{aligned}
A_{ij} &= e^{i\alpha(X_{\nu_i} + X_{\nu_j})} A_{ij}, \\
B_{ij} &= e^{i\alpha(X_{\nu_i} + X_{\nu_j} + X_S)} B_{ij}, \\
C_{ij} &= e^{i\alpha(X_{\nu_i} + X_{\nu_j} - X_S)} C_{ij}.
\end{aligned} \tag{3.7}$$

Therefore, texture (1) implies that

$$2X_{\nu_1} = 0, \quad X_{\nu_2} + X_{\nu_3} = 0, \tag{3.8}$$

while texture (4) results in

$$\begin{aligned}
X_{\nu_1} + X_{\nu_2} = 0, & \quad X_{\nu_1} + X_{\nu_3} = X_S, \\
X_{\nu_2} + X_{\nu_3} = -X_S, &
\end{aligned} \tag{3.9}$$

and so on. In addition to this, one of the following four conditions (see Ref. [18]):

$$X_S = \pm(X_{\Phi_1} - X_{\Phi_2}), \quad X_S = \pm \frac{1}{2}(X_{\Phi_1} - X_{\Phi_2}), \tag{3.10}$$

can be extracted from the scalar potential V_1 depending on which of the $a_{1,2,3,4}$ terms is invariant under the flavor $U(1)'$ symmetry. However, if only A has a nonzero texture then S is neutral under the flavor symmetry and the four conditions above are all automatically valid. In that case the cubic $a_{1,2}$ and quartic $a_{3,4}$ can simultaneously coexist.

B. Charged lepton sector

For the charged lepton sector, the same minimal textures already discussed in Ref. [19] and [18] apply, i.e.

$$\begin{aligned}
(1) \quad & \Pi_1: \begin{pmatrix} \times & 0 & 0 \\ 0 & \times & 0 \\ 0 & 0 & \times \end{pmatrix}, & \Pi_2: \begin{pmatrix} 0 & 0 & 0 \\ 0 & 0 & 0 \\ 0 & 0 & 0 \end{pmatrix}, \\
(2) \quad & \Pi_1: \begin{pmatrix} \times & 0 & 0 \\ 0 & \times & 0 \\ 0 & 0 & 0 \end{pmatrix}, & \Pi_2: \begin{pmatrix} 0 & 0 & 0 \\ 0 & 0 & 0 \\ 0 & 0 & \times \end{pmatrix}, \\
(3) \quad & \Pi_1: \begin{pmatrix} \times & 0 & 0 \\ 0 & 0 & 0 \\ 0 & 0 & 0 \end{pmatrix}, & \Pi_2: \begin{pmatrix} 0 & 0 & 0 \\ 0 & \times & 0 \\ 0 & 0 & \times \end{pmatrix}, \\
(4) \quad & \Pi_1: \begin{pmatrix} 0 & 0 & 0 \\ 0 & 0 & 0 \\ 0 & 0 & 0 \end{pmatrix}, & \Pi_2: \begin{pmatrix} \times & 0 & 0 \\ 0 & \times & 0 \\ 0 & 0 & \times \end{pmatrix}.
\end{aligned} \tag{3.11}$$

C. Dirac neutrino sector

For the Dirac neutrino textures, permutation of rows and columns are no longer independent from those in the charged lepton and Majorana neutrino sectors. As a result, besides fulfilling the constraint of M_D having a nonzero determinant, we must also consider textures that are equivalent up to permutations. In total, this amounts to six possible minimal combined textures,

$$\begin{aligned}
 1: & \begin{pmatrix} \times & 0 & 0 \\ 0 & \times & 0 \\ 0 & 0 & \times \end{pmatrix}, & 2: & \begin{pmatrix} \times & 0 & 0 \\ 0 & 0 & \times \\ 0 & \times & 0 \end{pmatrix}, & 3: & \begin{pmatrix} 0 & \times & 0 \\ \times & 0 & 0 \\ 0 & 0 & \times \end{pmatrix}, \\
 4: & \begin{pmatrix} 0 & \times & 0 \\ 0 & 0 & \times \\ \times & 0 & 0 \end{pmatrix}, & 5: & \begin{pmatrix} 0 & 0 & \times \\ \times & 0 & 0 \\ 0 & \times & 0 \end{pmatrix}, & 6: & \begin{pmatrix} 0 & 0 & \times \\ 0 & \times & 0 \\ \times & 0 & 0 \end{pmatrix},
 \end{aligned}$$

which in turn corresponds to 48 possible textures for $\Sigma_{1,2}$ —eight for each of the textures displayed above; 111, 112, 121, 211, 122, 212, 221, and 222, where the numbers indicate the corresponding nonzero entry in Σ_1 or Σ_2 . As an example, the eight possibilities for texture number 2 are given by

$$(111) \quad \Sigma_1: \begin{pmatrix} \times & 0 & 0 \\ 0 & 0 & \times \\ 0 & \times & 0 \end{pmatrix}, \quad \Sigma_2: \begin{pmatrix} 0 & 0 & 0 \\ 0 & 0 & 0 \\ 0 & 0 & 0 \end{pmatrix},$$

$$(112) \quad \Sigma_1: \begin{pmatrix} \times & 0 & 0 \\ 0 & 0 & \times \\ 0 & 0 & 0 \end{pmatrix}, \quad \Sigma_2: \begin{pmatrix} 0 & 0 & 0 \\ 0 & 0 & 0 \\ 0 & \times & 0 \end{pmatrix},$$

$$(121) \quad \Sigma_1: \begin{pmatrix} \times & 0 & 0 \\ 0 & 0 & 0 \\ 0 & \times & 0 \end{pmatrix}, \quad \Sigma_2: \begin{pmatrix} 0 & 0 & 0 \\ 0 & 0 & \times \\ 0 & 0 & 0 \end{pmatrix},$$

$$(211) \quad \Sigma_1: \begin{pmatrix} 0 & 0 & 0 \\ 0 & 0 & \times \\ 0 & \times & 0 \end{pmatrix}, \quad \Sigma_2: \begin{pmatrix} \times & 0 & 0 \\ 0 & 0 & 0 \\ 0 & 0 & 0 \end{pmatrix},$$

and so on for 122, 212, 221, 222.

D. Anomaly cancellation conditions

While global anomalies are typically regarded as benign, one must recall that the work previously developed in [19,32], which this article is based on, considers a local $U(1)'$ symmetry where gauge anomalies must necessarily be forbidden. With this in mind, and with the purpose of making the considered model consistent with a gauged version (to be studied elsewhere), one must also include a set of restrictions that incorporate the $U(1)'$ charges in the following triangle anomalies:

$$\begin{aligned}
 & [U(1)']^3, & U(1)'[\text{Gravity}]^2, \\
 & U(1)'[U(1)_{\text{Y}}]^2, & U(1)'[\text{SU}(2)_{\text{L}}]^2, \\
 & U(1)'[\text{SU}(3)_{\text{C}}]^2, & [U(1)']^2 U(1)_{\text{Y}}.
 \end{aligned} \tag{3.12}$$

As the right-handed neutrinos are solely charged under $U(1)'$, confer Table II, the only anomalies altered in comparison to [19] are those coming from $[U(1)']^3$ and $U(1)'[\text{Gravity}]^2$, i.e.

$$\begin{aligned}
 A_{U(1)'U(1)'U(1)'} & \equiv \sum_{i=1}^3 (6X_{q_i}^3 + 2X_{l_i}^3 - 3X_{u_i}^3 \\
 & \quad - 3X_{d_i}^3 - X_{e_i}^3 - X_{\nu_i}^3) = 0, \\
 A_{\text{gg}U(1)'} & \equiv \sum_{i=1}^3 (6X_{q_i} + 2X_{l_i} - 3X_{u_i} \\
 & \quad - 3X_{d_i} - X_{e_i} - X_{\nu_i}) = 0,
 \end{aligned} \tag{3.13}$$

where g denotes gravitational interactions while $A_{X,Y,Z} \propto \text{Tr}[T_X\{T_Y, T_Z\}]$ with T being the generators of the corresponding Lie Algebra. The remaining anomaly cancellation conditions are given in Eq. (A1). Overall, this results in a series of equations for anomaly cancellation, restricting the possible values of X_{Ψ_i} , from where one can extract all viable, anomaly free model versions.

E. Anomaly free solutions

Focusing on the solutions compatible with the BGL model, there are in total three anomaly free possibilities equipped with a type-I seesaw mechanism. These are denoted as $\nu\text{BGL-I}$, $\nu\text{BGL-IIa}$, and $\nu\text{BGL-IIb}$, being characterized by their lepton sector textures as follows:

(1) $\nu\text{BGL-I}$ Scenario

$$\begin{aligned}
 \Pi_1, \Sigma_1, B & = \begin{pmatrix} \times & \times & 0 \\ \times & \times & 0 \\ 0 & 0 & 0 \end{pmatrix}, & \Pi_2, \Sigma_2 & = \begin{pmatrix} 0 & 0 & 0 \\ 0 & 0 & 0 \\ 0 & 0 & \times \end{pmatrix}, \\
 A = 0, & \quad C = \begin{pmatrix} 0 & 0 & \times \\ 0 & 0 & \times \\ \times & \times & 0 \end{pmatrix}.
 \end{aligned} \tag{3.14}$$

(2) $\nu\text{BGL-IIa}$ Scenario

$$\begin{aligned}
 \Pi_1, \Sigma_1 & = \begin{pmatrix} \times & 0 & 0 \\ 0 & \times & 0 \\ 0 & 0 & 0 \end{pmatrix}, \\
 \Pi_2 & = \begin{pmatrix} 0 & 0 & 0 \\ \times & 0 & 0 \\ 0 & 0 & \times \end{pmatrix}, & \Sigma_2 & = \begin{pmatrix} 0 & \times & 0 \\ 0 & 0 & 0 \\ 0 & 0 & \times \end{pmatrix}, \\
 A & = \begin{pmatrix} \times & 0 & 0 \\ 0 & 0 & 0 \\ 0 & 0 & 0 \end{pmatrix}, & B & = \begin{pmatrix} 0 & 0 & 0 \\ 0 & 0 & \times \\ 0 & \times & 0 \end{pmatrix}, & C & = 0.
 \end{aligned} \tag{3.15}$$

TABLE I. Allowed charges for the various models. For model ν BGL-I and IIa we have $x_{tL} = -7x + 2y$ and $x_{tR} = -16x + 5y$. Model ν BGL-IIb has $x_{tL} = (-13x + 4y)/3$ and $x_{tR} = (-32x + 11y)/3$. In order for the BGL textures to be preserved, we additionally require that $y \neq 4x$.

Charges	ν BGL-I	ν BGL-IIa	ν BGL-IIb
q_L	$\begin{bmatrix} x \\ x \\ x_{tL} \end{bmatrix}$	\dots	\dots
u_R	$\begin{bmatrix} y \\ y \\ x_{tR} \end{bmatrix}$	\dots	\dots
d_R	$\begin{bmatrix} 2x - y \\ 2x - y \\ 2x - y \end{bmatrix}$	\dots	\dots
ℓ_L	$\begin{bmatrix} -3x \\ -3x \\ 21x - 6y \end{bmatrix}$	$\begin{bmatrix} x - y \\ -7x + y \\ 21x - 6y \end{bmatrix}$	$\frac{1}{3} \begin{bmatrix} -x - 2y \\ -17x + 2y \\ 39x - 12y \end{bmatrix}$
e_R	$\begin{bmatrix} -2x - y \\ -2x - y \\ 30x - 9y \end{bmatrix}$	$\begin{bmatrix} 2x - 2y \\ -6x \\ 30x - 9y \end{bmatrix}$	$\frac{1}{3} \begin{bmatrix} 2x - 5y \\ -14x - y \\ 58x - 19y \end{bmatrix}$
ν_R	$\begin{bmatrix} -4x + y \\ -4x + y \\ 12x - 3y \end{bmatrix}$	$\begin{bmatrix} 0 \\ -8x + 2y \\ 12x - 3y \end{bmatrix}$	$\frac{1}{3} \begin{bmatrix} -4x + y \\ -20x + 5y \\ 20x - 5y \end{bmatrix}$
Φ	$\begin{bmatrix} -x + y \\ -9x + 3y \end{bmatrix}$	$\begin{bmatrix} -x + y \\ -9x + 3y \end{bmatrix}$	$\frac{1}{3} \begin{bmatrix} 3(-x + y) \\ -19x + 7y \end{bmatrix}$
S	$8x - 2y$	$-4x + y$	$\frac{8x - 2y}{3}$

(iii) ν BGL-IIb Scenario

$$A = \begin{pmatrix} 0 & 0 & 0 \\ 0 & 0 & \times \\ 0 & \times & 0 \end{pmatrix}, \quad B = \begin{pmatrix} \times & 0 & 0 \\ 0 & 0 & 0 \\ 0 & 0 & 0 \end{pmatrix}, \quad C = \mathbf{0}, \quad (3.16)$$

where what distinguishes the ν BGL-IIa and ν BGL-IIb scenarios are the textures in the Majorana neutrino sector. Last but not least we show in Table I the generic $U(1)'$ charges for each of the BGL scenarios.

IV. CHOSEN SCENARIO

In what follows we will focus on the ν BGL-I scenario, whose allowed charges are constrained by the first column in Table I. We make this choice after having investigated the other possibilities available within this model and verified that the ν BGL-I scenario is the one for which our numerical analysis and parameter space scans were more efficient. This, of course, does not exclude the possible interest of the other scenarios, but our main goal is to understand the typical phenomenology of this class of models. Thus, for ν BGL-I, choosing $x = 1$ and $y = 1/3$ the model considered in this article is then defined by the quantum numbers in Table II.

Notice that the assigned quantum numbers for the up-type quarks can also be flipped in such a way that there are in total three variations of the ν BGL-I scenario. This depends, in practice, on the choice of up-type quark associated with the Δ_2 matrix in Eq. (2.2) and the designation of the model is typically associated with that, i.e. variation u , c , or t . In the remainder of this article we focus on variation t .

As already stated, one of the novel features of the model considered is the presence of three generations of right-handed neutrinos. In order to comply with experimental data a realistic lepton mixing and neutrino mass hierarchy must be assured. Both the charged neutral sectors can be rotated to the mass basis via biunitary matrices, that is,

$$M_L^{\text{diag}} = U_L^\dagger M_L U_R, \quad M_\nu^{\text{diag}} = U_\nu^\dagger M_\nu U_\nu, \quad (4.1)$$

where M_L is a 3×3 matrix expressed in the basis $\{e_L^1, e_L^2, e_L^3\} \otimes \{e_R^1, e_R^2, e_R^3\}$ as usual, while M_ν is a 6×6

TABLE II. Charge assignments of the $SU(2)$ scalar doublets and SM fermions under the flavor symmetry $U(2)'$ and the SM gauge group, $SU(3)_C \times SU(2)_L \times U(1)_Y$. The corresponding $U(1)'$ charges are computed using the formulas from the first column of Table I taking $x = 1$ and $y = 1/3$.

	Φ_1	Φ_2	S	q_1	q_2	q_3	u_{R_1}	u_{R_2}	u_{R_3}	d_{R_1}	d_{R_2}	d_{R_3}
$U(1)_Y$	1/2	1/2	0	1/6	1/6	1/6	2/3	2/3	2/3	-1/3	-1/3	-1/3
$SU(2)_L$	2	2	1	2	2	2	1	1	1	1	1	1
$SU(3)_C$	1	1	1	3	3	3	3	3	3	3	3	3
$U(1)'$	-2/3	-8	22/3	1	1	-19/3	1/3	1/3	-43/3	5/3	5/3	5/3

	ℓ_1	ℓ_2	ℓ_3	e_{R_1}	e_{R_2}	e_{R_3}	ν_{R_1}	ν_{R_2}	ν_{R_3}
$U(1)_Y$	-1/2	-1/2	-1/2	-1	-1	-1	0	0	0
$SU(2)_L$	2	2	2	1	1	1	1	1	1
$SU(3)_C$	1	1	1	1	1	1	1	1	1
$U(1)'$	-3	-3	19	-7/3	-7/3	27	-11/3	-11/3	11

matrix written in the basis $\{\nu_L^1, \nu_L^2, \nu_L^3, \nu_R^1, \nu_R^2, \nu_R^3\}$. On the other hand, U_L , U_R , and U_ν are unitary matrices. We can then define the PMNS matrix as

$$V_P = U_L^\dagger P U_\nu = (V_{\text{PMNS}}^{\text{SM}} \mathcal{O}_P), \quad P = (\mathbb{1}_{3 \times 3} | 0_{3 \times 3}), \quad (4.2)$$

where V_P is a 3×6 matrix with the first 3×3 entries encoding the SM charged-lepton and neutrino interactions, and \mathcal{O}_P contains the interactions between leptons and the heavy neutrinos. In our analysis we require $\mathcal{O}_P < 10^{-5}$ such that charged currents involving active and Beyond Standard Model (BSM) neutrinos are suppressed. Also, we require the masses of such active neutrinos to be between $[0, 10^{-9}]$ GeV while their heavy counterparts have masses around the TeV scale. While an in-depth study of neutrino physics is beyond the scope of this work, we have performed a fit to the light neutrino masses in order to respect the normal hierarchy [35],

$$\begin{aligned} M_{\nu_2}^2 - M_{\nu_1}^2 &\approx 10^{-5} \text{ eV}^2, \\ M_{\nu_3}^2 - M_{\nu_2}^2 &\approx 10^{-3} \text{ eV}^2. \end{aligned} \quad (4.3)$$

This was numerically required for all points that pass the theoretical and experimental constraints, as it will be discussed in upcoming sections. Although a full fit was not done across the entirety of the parameter space, and given that our studies of the scalar and quark sectors are independent of neutrino physics, we have confirmed and can safely argue that the discussed model is compatible with neutrino data.

A. Inversion procedure for the scalar sector

Following the same methodology used previously in [34], our goal is to provide the physical masses and mixing angles as inputs and then search for valid regions in the parameter space. In the considered $\nu\text{BGL-I}$ scenario the scalar potential is given in Eq. (2.16) with $a_3, a_4 = 0$. Selecting a vacuum configuration with real VEVs (v_1, v_2, v_S) , one obtains the following minimization conditions:

$$\begin{aligned} \mu_1^2 &= -\left(v_1^2 \lambda_1 + \frac{v_S^2 \lambda'_2}{2} + \frac{v_2 \hat{\mu}}{2v_1}\right), \\ \mu_2^2 &= -\left(v_2^2 \lambda_2 + \frac{v_S^2 \lambda'_3}{2} + \frac{v_1 \hat{\mu}}{2v_2}\right), \\ \mu_S^2 &= -\frac{\sqrt{2}v_1 v_2 (a_1 + a_2) + v_S (v_1^2 \lambda'_2 + v_2^2 \lambda'_3 + 2v_S^2 \lambda'_1 + 2\mu_b^2)}{2v_S}, \end{aligned} \quad (4.4)$$

where one defines

$$\hat{\mu} = v_S \sqrt{2}(a_1 + a_2) + v_1 v_2 (\lambda_3 + \lambda_4) + 2\mu_3^2. \quad (4.5)$$

The physical scalar spectrum contains three CP -even scalars $H_{1,2,3}$, two pseudoscalars $A_{2,3}$, and one charged Higgs boson H^\pm . In a configuration close to the vacuum alignment in one of the Higgs doublets, the corresponding CP -even scalar corresponds to the SM Higgs boson with mass 125.09 GeV and with SM-like interactions to the gauge bosons and fermions. Notice that, if such interactions coincide with the SM ones, one often refers to it as the exact alignment limit. However, direct searches for new scalars [36–41] still keep a window opened for possible off-alignment deviations that we consider in our analysis below. In order to keep the physical parameters of the theory under control one performs an inversion procedure analogous to that developed in [34], expressing the parameters of the scalar potential in Eq. (4.4) in terms of physical masses, mixing angles (including the Higgs alignment parameter) and VEVs as we discuss in what follows.

First, the matrix \mathcal{O}_β , which rotates the gauge eigenstates into the Higgs basis,³ is introduced

$$\mathcal{O}_\beta = \begin{pmatrix} \cos \beta & \sin \beta & 0 \\ -\sin \beta & \cos \beta & 0 \\ 0 & 0 & 1 \end{pmatrix} = \begin{pmatrix} v_1/v & v_2/v & 0 \\ -v_2/v & v_1/v & 0 \\ 0 & 0 & 1 \end{pmatrix}, \quad (4.6)$$

where one defines

$$\begin{aligned} v_1 &= v \cos \beta, \\ v_2 &= v \sin \beta, \\ v &= \sqrt{v_1^2 + v_2^2} \approx 246 \text{ GeV}. \end{aligned} \quad (4.7)$$

Starting with the scalar potential in Eq. (2.15) and expanding it using the field definitions in Eq. (2.3), the CP -odd sector mass matrix can be obtained as

$$\frac{1}{2} \begin{pmatrix} I_1 & I_2 & \eta \\ I_2 & I_2 & \eta \\ \eta & \eta & \eta \end{pmatrix} \mathcal{M}_S^2 \begin{pmatrix} I_1 \\ I_2 \\ \eta \end{pmatrix}. \quad (4.8)$$

Using \mathcal{O}_β one can rotate \mathcal{M}_S^2 to the Higgs basis, where it acquires a block-diagonal form

$$\mathfrak{M}_S^2 = \mathcal{O}_\beta \mathcal{M}_S^2 \mathcal{O}_\beta^T. \quad (4.9)$$

We can further diagonalize \mathfrak{M}_S^2 via an additional rotation matrix \mathcal{O}_γ as

³The Higgs basis corresponds to a redefinition of the physically equivalent doublets so that only one of them contains a VEV.

$$\begin{pmatrix} 0 & 0 & 0 \\ 0 & M_{A_2}^2 & 0 \\ 0 & 0 & M_{A_3}^2 \end{pmatrix} = \mathcal{O}_\gamma \mathfrak{M}_S^2 \mathcal{O}_\gamma^T = \mathcal{O}_\gamma \mathcal{O}_\beta \mathcal{M}_S^2 \mathcal{O}_\beta^T \mathcal{O}_\gamma^T, \quad (4.10)$$

where one defines

$$\mathcal{O}_\gamma = \begin{pmatrix} 1 & 0 & 0 \\ 0 & \cos \gamma_1 & -\sin \gamma_1 \\ 0 & \sin \gamma_1 & \cos \gamma_1 \end{pmatrix}. \quad (4.11)$$

Notice that while the neutral CP -odd Goldstone boson can be gauged away from the particle spectrum and gets absorbed as the longitudinal polarization of the Z^0 boson, one of the two physical pseudoscalars is in fact a pseudo-Goldstone state that emerges due to both spontaneous and explicit breaking of the global $U(1)'$ symmetry.

Similarly, the CP -even states can be rotated to the mass basis as

$$\begin{pmatrix} M_{H_1}^2 & 0 & 0 \\ 0 & M_{H_2}^2 & 0 \\ 0 & 0 & M_{H_3}^2 \end{pmatrix} = \mathcal{O}_\alpha \mathcal{O}_\beta \mathcal{M}_H^2 \mathcal{O}_\beta^T \mathcal{O}_\alpha^T, \quad (4.12)$$

with

$$\mathcal{O}_\alpha = R_3 \cdot R_2 \cdot R_1 \quad (4.13)$$

and

$$\begin{aligned} R_1 &= \begin{pmatrix} \cos \alpha_1 & -\sin \alpha_1 & 0 \\ \sin \alpha_1 & \cos \alpha_1 & 0 \\ 0 & 0 & 1 \end{pmatrix}, \\ R_2 &= \begin{pmatrix} \cos \alpha_2 & 0 & \sin \alpha_2 \\ 0 & 1 & 0 \\ -\sin \alpha_2 & 0 & \cos \alpha_2 \end{pmatrix}, \\ R_3 &= \begin{pmatrix} 1 & 0 & 0 \\ 0 & \cos \alpha_3 & \sin \alpha_3 \\ 0 & -\sin \alpha_3 & \cos \alpha_3 \end{pmatrix}. \end{aligned} \quad (4.14)$$

The presence of a CP -even state behaving as a SM-like Higgs boson is ensured not only requiring that

$$M_{H_1} = 125.09 \text{ GeV}, \quad (4.15)$$

but also that the couplings to fermions and gauge bosons of this particle closely reproduce the SM predictions, which are controlled by the coupling modifier

$$[\mathcal{O}_\alpha \mathcal{O}_\beta]_{12} = -\cos \alpha_2 \sin \delta \quad \text{with} \quad \delta \equiv \alpha_1 - \beta, \quad (4.16)$$

such that the coupling of the 125 GeV Higgs boson to the electroweak gauge bosons can be expressed as

$$\lambda'_{hVV} = -\lambda_{hVV}^{\text{SM}} \cos \alpha_2 \sin \delta, \quad (4.17)$$

with $\lambda_{hVV}^{\text{SM}}$ denoting the SM Higgs boson coupling to gauge bosons, $V = Z, W$ in the SM. This means that the alignment condition concerning Higgs gauge interactions is governed not by a single angle but instead two angular parameters, δ and α_2 . Furthermore, as the LHC has been putting stringent limits on deviations from the SM, one expects that $\cos \alpha_2 \sin \delta \sim \mathcal{O}(1)$, i.e. δ must not be far from $\pi/2$ while α_2 must be small. Note also that Eq. (4.16) ensures that the interactions of the SM-like Higgs boson are dominantly inherited from the second doublet which is the one that couples to the top-quark. Further conditions for alignment will be obtained from the Higgs' interactions with fermions. For instance, given that the top mass in this model comes only from the matrix Δ_2 , it will be proportional to v_2 and therefore the coupling modifier for the Higgs-top interactions will be

$$\lambda'_{h\bar{t}t} = -\lambda_{h\bar{t}t}^{\text{SM}} \frac{\cos \alpha_2 \sin \delta}{\sin \beta}. \quad (4.18)$$

With $\sin \delta = \sin(\alpha_1 - \beta) \sim \mathcal{O}(1)$ as mentioned earlier, we see that a further condition for alignment is $\cos \alpha_2 \simeq -\sin \beta \simeq -\cos \alpha_1$. Additional conditions would be obtained from analyzing the remaining Higgs-fermion interactions. Notice that the minus signs present in Eqs. (4.16) and (4.18) are not necessarily meaningful. We know, from the measured Higgs diphoton branching ratio at the LHC, that the relative sign of $\lambda'_{h\bar{t}t}$ and λ'_{hWW} ought to be the same as that of $\lambda_{h\bar{t}t}^{\text{SM}}$ and $\lambda_{hWW}^{\text{SM}}$. An overall minus sign affecting both couplings can therefore be physically meaningless. In our numerical analysis of the next section, however, we took into account all possible relative signs, and compared the predicted Higgs branching ratios and production cross sections with the known experimental values, thus ensuring that, whatever relative signs there may be between Higgs couplings in this model, the LHC constraints are satisfied.

Last but not least, the charged Higgs sector contains only one physical scalar as the charged Goldstone boson is gauged away from the particle spectrum and plays a role of the longitudinal polarization of the W^\pm boson. In particular, the mass form reads as

$$\begin{pmatrix} 0 & 0 \\ 0 & M_{H^\pm}^2 \end{pmatrix} = \mathcal{O}'_\gamma \mathcal{O}'_\beta \mathcal{M}^\pm \mathcal{O}'_\beta{}^T \mathcal{O}'_\gamma{}^T \quad (4.19)$$

with

TABLE III. Parameter intervals used in numerical scans.

Parameter	$\alpha_2, \alpha_3, \gamma_1$	$\tan\beta$	δ	a_3, a_4
Range	$[-\pi, \pi]$	$[0.5, 30]$	$[\frac{\pi}{2} - 1, \frac{\pi}{2} + 1]$	0
Parameter	M_{A_2}, M_{H^\pm}	M_{A_3}	M_{H_2}, M_{H_3}	a_2
Range (GeV)	$[0.5, 1600]$	$[30, 2000]$	$[126, 1800]$	$[-1, 1]$

$$\mathcal{O}'_\beta = \begin{pmatrix} \cos\beta & \sin\beta \\ -\sin\beta & \cos\beta \end{pmatrix}, \quad \mathcal{O}'_\gamma = \begin{pmatrix} \cos\gamma_2 & \sin\gamma_2 \\ -\sin\gamma_2 & \cos\gamma_2 \end{pmatrix}. \quad (4.20)$$

The inversion procedure described above is applied to the scalar sector with the purpose of trading the quartic couplings for physical masses and mixing angles. The corresponding analytical formulas are lengthy and can be found in Appendix B. In our numerical analysis, the physical masses $M_{H_1}, M_{H_2}, M_{H_3}, M_{A_2}, M_{A_3}, M_{H^\pm}$, the angles $\beta, \alpha_1, \alpha_2, \alpha_3, \gamma_1, \gamma_2$, and the cubic couplings a_1, a_2, a_3 are then used as input parameters limited to be randomly sampled within physically reasonable ranges as detailed below in Sec. V.

V. PARAMETER SPACE AND PHENOMENOLOGICAL CONSTRAINTS

The parameter space scan discussed in this section relies on the inversion procedure described previously, where both scalar masses and mixing angles are used as input, allowing one to determine the gauge eigenbasis couplings of the Higgs potential in Eq. (2.16). The ranges used in the scan can be found in Table III. According to the discussion below Eq. (4.17), the chosen scanning ranges for δ are centered around $\pi/2$ where $\sin\delta = 1$. While α_2 must be small, we let it range between $-\pi$ and π in order to let $\cos\alpha_2$ capture both positive and negative values. Furthermore, the somewhat large ranges set for both δ

and α_2 were deliberately picked in order to ensure that the allowed off-alignment regions are entirely covered in the numerical analysis, as we discuss further ahead. It is also worth mentioning that the SM-like Higgs boson was chosen to be the lightest of the CP -even scalars and the absolute value of the cubic couplings is such that $|a_2| \leq 1$.

Using the inversion procedure we then extract the Lagrangian parameters and feed them to SPheno [28] in order to calculate both the STU electroweak precision observables (or oblique parameters) as well as Higgs decay widths and branching fractions. The most up to date electroweak fit for the STU parameter [42] can be summarized as

$$\begin{aligned} S &= -0.01 \pm 0.10 \\ T &= 0.03 \pm 0.12 \\ U &= 0.02 \pm 0.11 \end{aligned}, \quad \rho_{ij} = \begin{pmatrix} 1 & 0.92 & -0.80 \\ 0.92 & 1 & -0.93 \\ -0.80 & -0.93 & 1 \end{pmatrix}, \quad (5.1)$$

with ρ_{ij} denoting a 92% correlation between S and T, while U-S and U-T are 80% and -93% anticorrelated, respectively. For the purpose of this analysis, we required $\Delta\chi^2 < 7.815$, which translates into a 95% confidence level (CL) agreement with the electroweak fit, where

$$\Delta\chi^2 = \sum_{ij} (\Delta\mathcal{O}_i - \Delta\mathcal{O}_i^{(0)}) [(\sigma^2)^{-1}]_{ij} (\Delta\mathcal{O}_j - \Delta\mathcal{O}_j^{(0)}), \quad (5.2)$$

with $[\sigma^2]_{ij} \equiv \sigma_i \rho_{ij} \sigma_j$ the covariance matrix and σ_i the standard deviations in Eq. (5.1). The notation employed here is such that $\Delta\mathcal{O}_i^{(0)}$ indicates the S, T, U experimental fit values, while $\Delta\mathcal{O}_i$ denotes the S, T, U calculated values in SPheno. In Fig. 1 we show the points that pass the STU restrictions with a CL of, at least, 95% (blue shades) in comparison with the points that are excluded (gray). The color bar represents the $\Delta\chi^2$ values. The majority of points that were simulated are rejected due to large T values, as anticipated. However, one of the benefits of 2HDM-like models is that

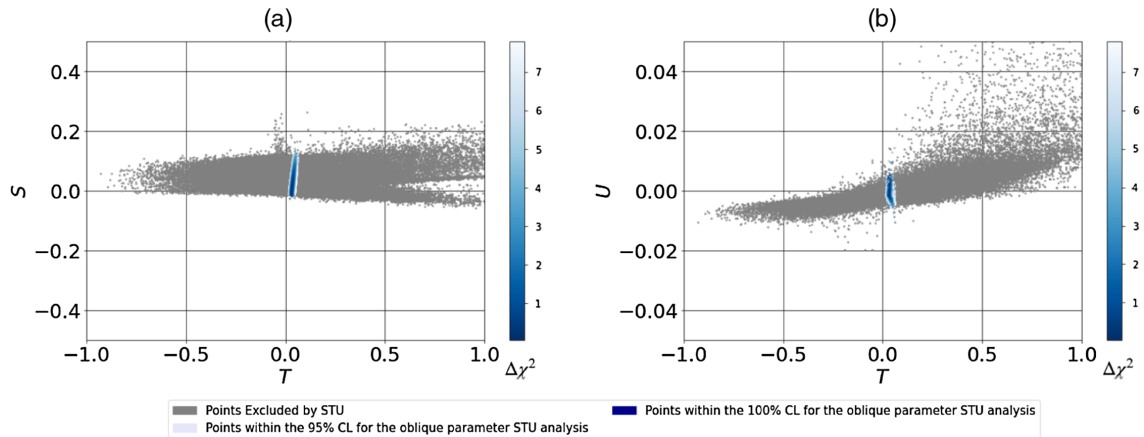


FIG. 1. Electroweak precision observables for all simulated points. The colored points are those who pass the STU analysis with a confidence level (CL) of at least 95%. Gray points are excluded by precision EW fit data.

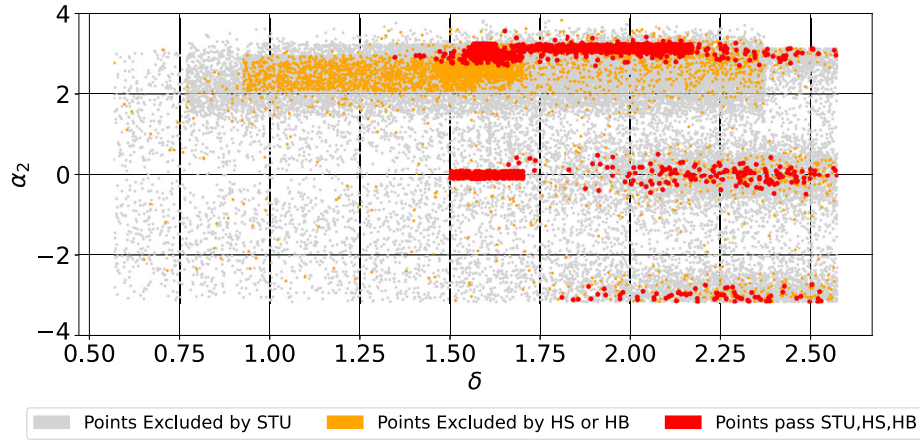


FIG. 2. Angles entering in the Higgs coupling modifier of Eq. (4.17). Gray points are excluded by EW precision observables while orange ones pass the STU $\Delta\chi^2$ test but fail Higgs physics constraints. Red points pass all restrictions and represent the regions where the Higgs boson is closely aligned with a SM-like one.

there are parameter space regions for which all constraints on the oblique parameters are satisfied, as is the case here. While the STU analysis offers a strong razor of the parameter space, it is still necessary to match these points to both Higgs and flavor observables. First, let us focus on the impact of Higgs physics leaving the flavor analysis for later. In Fig. 2, we show the allowed regions in the δ - α_2 plane that survive not only the EW precision tests but also that comply with the properties of

a SM-like Higgs boson and are not excluded by direct searches for new scalars at the LHC. As usual, this is done by using the SPheno output SLHA files as input cards to HiggsSignals (HS) and HiggsBounds (HB) [29,30] for every single point that passes the STU test.

The points that survive both HS and HB are shown in red and were found to pile in a region around that of the exact alignment limit where $\delta = \pi/2$ and $\alpha_2 = -\pi, 0, \pi$. In

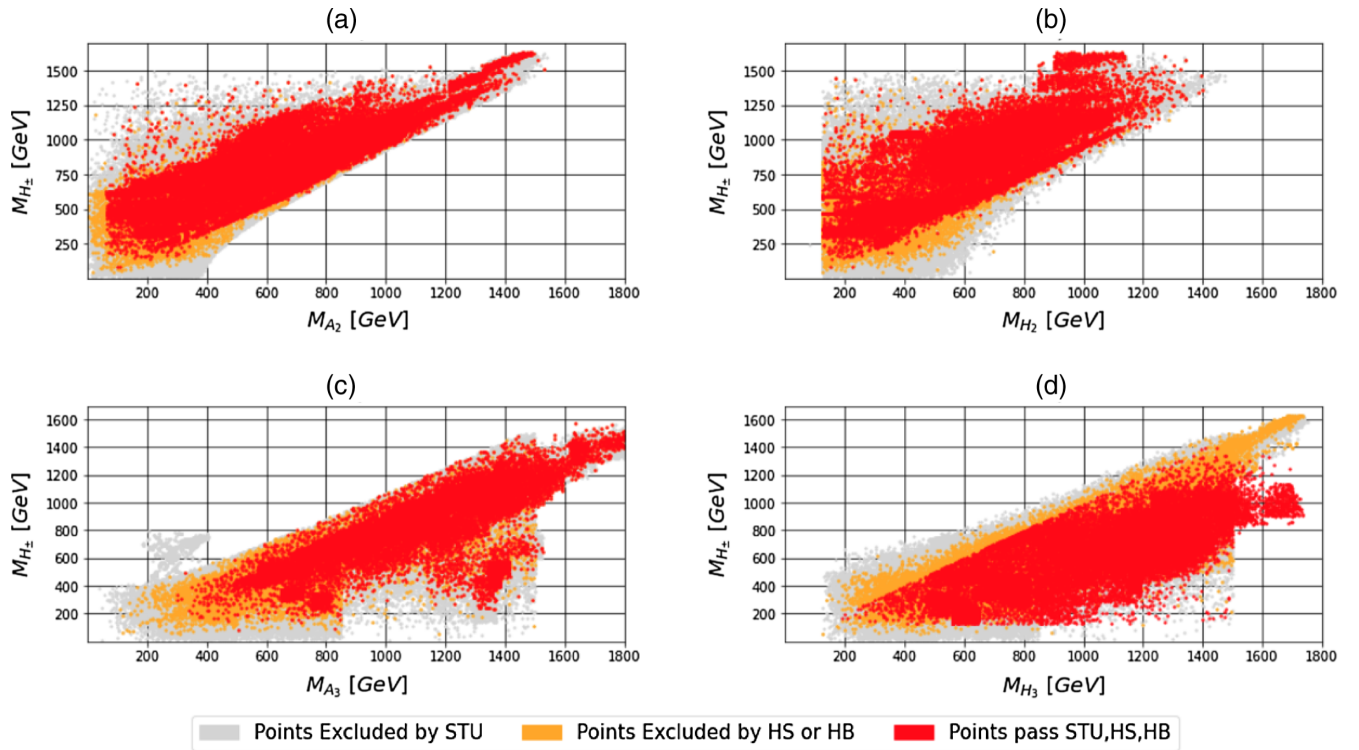


FIG. 3. Mass of the charged Higgs versus the masses of the pseudoscalars A_2 and A_3 (left panels) and of the CP -even scalars H_2 and H_3 (right panels). Gray points are excluded by the oblique STU parameters, orange points are excluded either by HB or HS, while simultaneously passing the STU restrictions. Red points pass all constraints.

TABLE IV. Most relevant quark flavor violation (QFV) observables. The first column represents the prediction of the SM for each observable, the second column indicates the 1σ error of the SM theoretical calculation, the third column is the measured experimental value, the fourth is the 1σ experimental error, and the last column is this measured deviation between the SM prediction and the observed value from experiment.

Channel	\mathcal{O}_{SM}	σ_{SM}	\mathcal{O}_{Exp}	σ_{Exp}	σ
$\text{BR}(B \rightarrow \chi_s \gamma)$	3.29×10^{-4}	1.87×10^{-5}	3.32×10^{-4}	0.16×10^{-4}	0.075
$\text{BR}(B_s \rightarrow \mu\mu)$	3.66×10^{-9}	1.66×10^{-10}	2.80×10^{-9}	0.06×10^{-9}	0.038
ΔM_d (GeV)	3.97×10^{-13}	5.07×10^{-14}	3.33×10^{-13}	0.013×10^{-13}	0.11
ΔM_s (GeV)	1.24×10^{-11}	7.08×10^{-13}	1.17×10^{-11}	0.0014×10^{-11}	0.054
ϵ_K (GeV)	1.81×10^{-3}	2.00×10^{-4}	2.23×10^{-3}	0.011×10^{-3}	0.14

particular, we found that deviations from an exact alignment are primarily driven by the δ angle which can vary in a wider range, whereas α_2 is tightly constrained in the aforementioned regions, with $0.60 < -\cos \alpha_2 \sin \delta < 1.0$ for the upper red island, $0.60 < \cos \alpha_2 \sin \delta < 0.99$ in the middle region, and $0.60 < -\cos \alpha_2 \sin \delta < 0.98$ at the $\alpha_2 = -\pi$ line. In Fig. 3 we show the dependence of the charged Higgs boson mass M_{H^\pm} in terms of the masses of the A_2 and A_3 pseudoscalars (left panels) as well as of the masses of the non-SM CP -even states H_2 and H_3 (right panels). The color scheme is the same as in Fig. 2 and, as the red region demonstrates, we have obtained valid points that cover a wide range of masses for new scalars. In particular, there are viable solutions with charged Higgs bosons that can be as light as approximately 100 GeV extending all the way up to about 1.6 TeV, the light pseudoscalar is limited to the range that goes from 100 GeV up to 1.5 TeV while its heavy counterpart is heavier than 300 GeV but lighter than 1.8 TeV. For the CP -even sector, besides a SM-like state with mass 125.09 GeV, one finds that H_2 is sharply limited from below at the Higgs boson mass, i.e. 125.09 GeV, allowing valid solutions up to approximately 1.4 TeV, while its heavy partner mass ranges between 200 GeV and approximately 1.7 TeV. Note that the limits above must be understood in the context of a search of the parameter space dedicated to find light scalars. In fact, the low mass region is particularly interesting from the collider physics perspective and can potentially be tested in the near future.

Besides electroweak and Higgs physics constraints, one also has to confront the generated data with quark flavor violation (QFV) observables. According to the textures of the chosen $\nu\text{BGL-I}$ scenario, the most stringent constraints are on the down-type quark sector rather than in the up-quark or charged lepton ones. Notice also that the most stringent QFV restrictions are indeed coming from processes involving down-type quarks, in particular those shown in Table IV. We show in Fig. 4 the individual impact that each of the considered QFV observable poses to the points that have survived the electroweak and Higgs physics constraints. The color scheme is identical to that in

Figs. 2 and 3 with the inclusion of green points that represent points simultaneously allowed by EW, Higgs, and QFV observables. It is promptly noticeable that both ϵ_K , panel (c), and $\text{BR}(B \rightarrow \chi_s \gamma)$, panel (a), represent the weaker flavor physics constraints on the parameter space in such a way that all of the points that have survived the EW and Higgs physics constraints are also compatible with these two QFV observables. On the other hand, ΔM_s , panel (b), ΔM_d , panel (e), and $\text{BR}(B_s \rightarrow \mu\mu)$, panel (d), place a noticeable veto on the allowed parameter space. ΔM_s is the main culprit, with the lowest number of allowed points that survive such a constraint. We also note that both ΔM_d and ΔM_s limit the mass to be below 1 TeV for the A_2 pseudoscalar. Indeed, the low mass regime is where the vast majority of the allowed points tend to accumulate. For a cleaner analysis we show in the histograms of Fig. 5 the number of points that are allowed by ΔM_s , ΔM_d , $\text{BR}(B_s \rightarrow \mu\mu)$ and combinations of them, in bins of the lightest pseudoscalar mass. We also show in Table V the acceptance ratio, defined as the percentage of the initial sample consistent with EW and Higgs physics that also survives a certain QFV cut, for each of the considered QFV observables as well as the three combinations in Fig. 5. Our results reveal that the sharpest razor of the parameter space is the combination of $\text{BR}(B_s \rightarrow \mu\mu)$ and ΔM_s with a very low acceptance ratio of only 9.39%, while their individual contributions are 35% and 26%, respectively. This combination of observables also prefers pseudoscalar masses to be in a range between 125 GeV and 1300 GeV. However, such a limited range must not be regarded as a particular feature of the $\nu\text{BGL-I}$ model but merely as a result of the numerical scan, which is only efficient if all scalar masses are sufficiently light.⁴ Indeed, it is well known that multi-Higgs models typically observe a decoupling limit when the masses of the new scalars tend to

⁴When using an inversion procedure that receives as input parameters only physical masses and mixing angles, large hierarchies between the Higgs boson mass and the remaining scalars often result in unacceptably large values for the quartic couplings, which can be as large as several tenths of thousands.

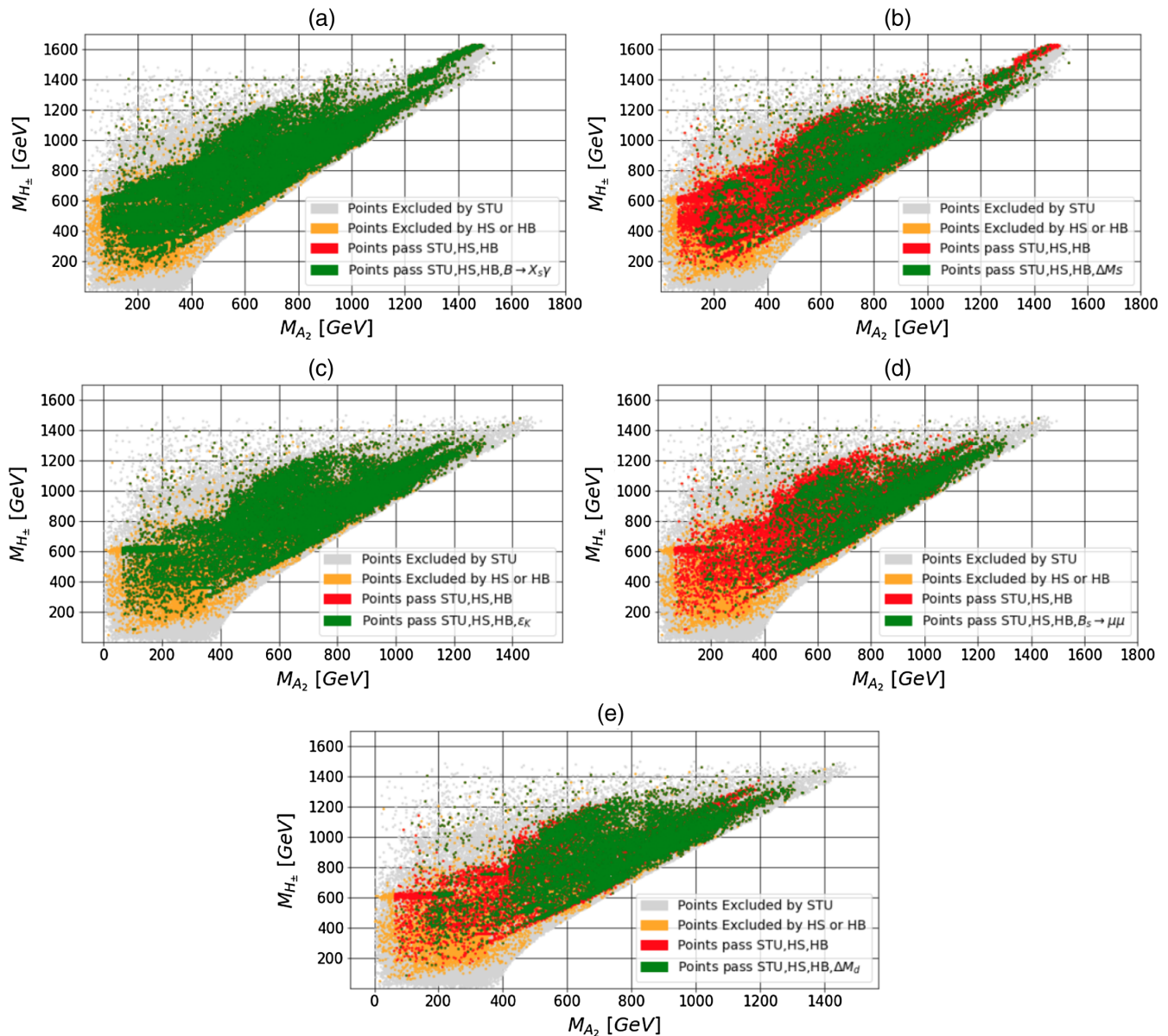


FIG. 4. Mass of the charged Higgs versus the mass of the lightest pseudoscalar A_2 . Gray points are excluded by STU observables, orange points are excluded by HS or HB while still passing STU, and red points pass STU, HS, and HB constraints. In green, we showcase the points that pass a given QFV observable, namely, we have (a) $B \rightarrow \chi_s \gamma$, (b) ΔM_S , (c) ϵ_K , (d) $B_s \rightarrow \mu\mu$, and (e) ΔM_d , while passing STU, HB, and HS constraints.

infinity. Therefore, the study of parametric regions with large scalar masses requires a different strategy to increase the acceptance ratio as, e.g. it was done in [34] by forcing the exact alignment limit and providing only the Higgs boson mass as input. For a closer inspection we show in Fig. 6 two of the QFV observables of Table IV in terms of the charged Higgs and heavier pseudoscalar masses. For a moment we ignore the EW and Higgs physics constraints and show in gray the points that are excluded by at least one QFV observable while the colored points are simultaneously allowed by all the QFV restrictions. Note that, even

considering the entire universe of sampled points there are only two points outside the $\pm 2\sigma$ uncertainty band (dashed lines) that would fail $\text{BR}(B \rightarrow \chi_s \gamma)$ (right panel) while $\text{BR}(B_s \rightarrow \mu\mu)$ is visibly rather more restrictive (left panel). It is also clear that larger scalar masses tend to relax the QFV constraints as expected.

Last but not least, we show in Fig. 7 the combination of all EW, Higgs, and flavor physics constraints. We have considered the four mostly stringent QFV observables in Table IV, leaving out only ϵ_K as it adds the least amount of constraints to our model. It is clear that the majority of

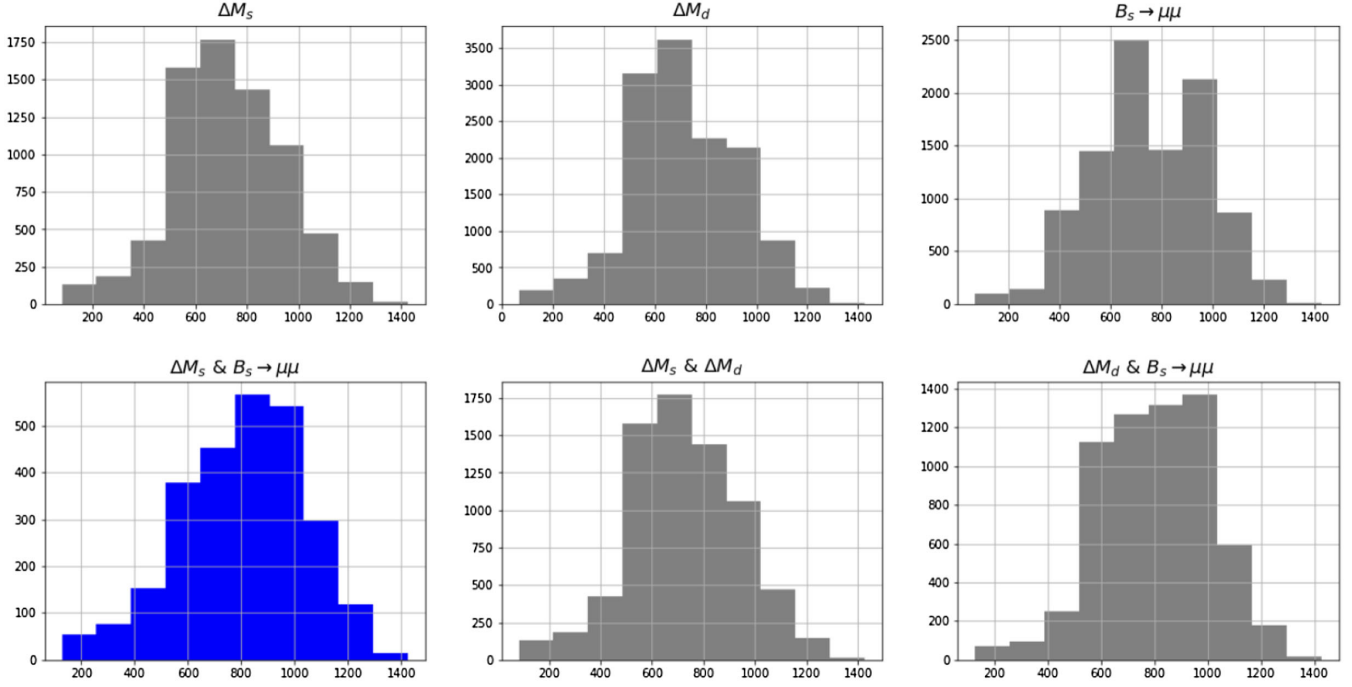


FIG. 5. Histograms containing points that survive STU, HS, HB, and a given QFV (or pair of) in bins of the A_2 mass. The most restrictive is colored in blue.

sampled points fall in the dark gray area where at least one of the considered QFV observables lies beyond the 2σ uncertainty range limited by the blue dashed lines. As one can also see, flavor physics plays the major role in strongly reducing the allowed parameter space. In particular, for points complying with a 2σ uncertainty of all QFV observables (within the two blue dashed curves), we note that the majority of allowed cases also prefer the charged Higgs boson mass to be in a range between 400 GeV and 1.4 TeV. If we further demand that all QFV observables are simultaneously reproduced within their 1σ bound, then the viable region, identified by the cyan points, tends to be further compressed. Once again, it is important to mention that our scan was optimized to the low mass region, becoming increasingly inefficient with increasing scalar

masses. Therefore one cannot extract bold conclusions about the high mass regime. On the contrary, what is important to retain as a key result of this article is that the ν BGL-I model is compatible with the current EW, Higgs, and QFV observables in the limit where new scalar masses are near the EW-scale. This opens up the possibility for testing the model in a foreseeable future, potentially already at the LHC run-III, as discussed below.

VI. PHENOMENOLOGY AT THE LHC

In this section we compare the points that have survived all constraints with current direct $\tau\tau$ [43], ZZ [40] and WW [44] final states. An interface between SPheno and MadGraph [45] allows one to determine the neutral scalar production cross section times its decay branching ratio to a given final state.

In Fig. 8 we show the latest ATLAS limits for scalar and pseudoscalar searches in the ditau final state and confront them with our prediction for the lighter BSM Higgs bosons H_2 and A_2 . The green (cyan) points have the same meaning as in Fig. 7, i.e. they are points for which the measured values of the considered QFV observables are reproduced in our calculation within a 2σ (1σ) uncertainty. As one can observe, all points comfortably sit within the bounds set after the ATLAS run-II search. One may also take note that the calculated cross sections in the ν BGL-I model can become fairly small, even for masses close to the EW scale, although various points with sizable cross sections are

TABLE V. Acceptance ratio for each QFV (first five rows) and for pairs of QFV variables (last three rows). The most restrictive set is marked in blue.

Set of QFV observables	Acceptance ratio
$BR(B \rightarrow \chi_s \gamma)$	100.0%
$BR(B_s \rightarrow \mu\mu)$	35.0%
ΔM_d (GeV)	48.0%
ΔM_s (GeV)	26.0%
ϵ_K (GeV)	100.0%
$BR(B_s \rightarrow \mu\mu)$ & ΔM_s	9.39%
$BR(B_s \rightarrow \mu\mu)$ & ΔM_d	22.21%
ΔM_s & ΔM_d	25.57%

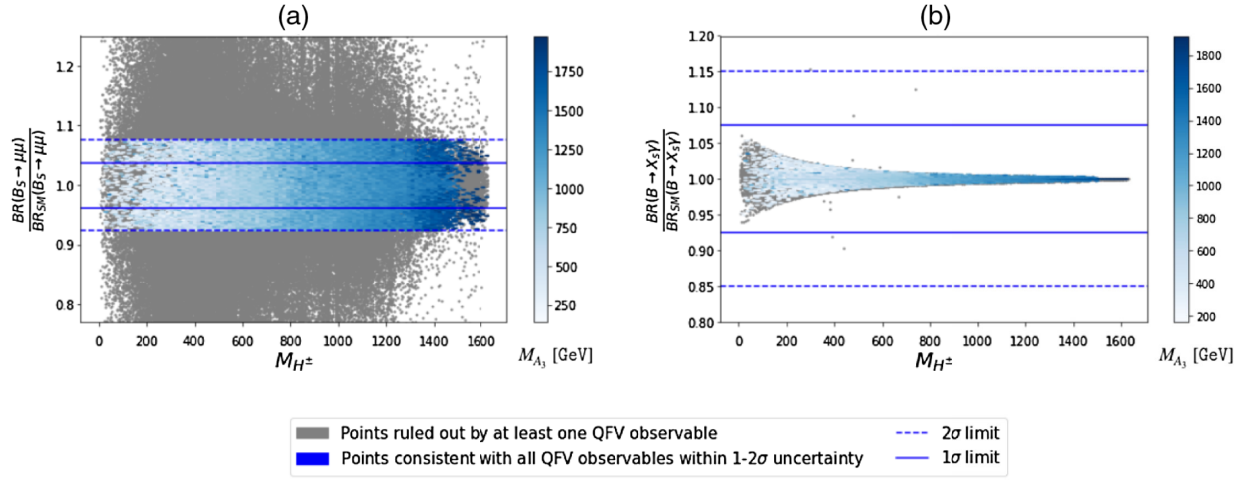


FIG. 6. Plots of the ratio between the BR for the decays $B_S \rightarrow \mu^+\mu^-$ (on the left) and $B \rightarrow X_s\gamma$ (on the right) computed in the ν BGL-I model and in the SM versus the mass of the charged scalar. In the color bar, we showcase the mass of the heaviest pseudoscalar A_3 . Gray points are excluded from at least one QFV observable from IV at a 2σ uncertainty. Dashed blue lines indicate the 2σ bound and full blue lines indicate the 1σ limit.

present. For the H_2 gluon-fusion production mechanism (Fig. 8), a point with the largest signal strength was found to be 0.083 pb, which can be probed in future LHC runs. An estimation of the expected number of events at the high-luminosity (HL) phase of the LHC, with $\mathcal{L} = 3000 \text{ fb}^{-1}$, leads to $N = \sigma\mathcal{L} \sim 249078$, whereas for run-III luminosities one expects $N \sim 24907$. This suggests that the low H_2

mass regime can potentially be tested already with run-III data in the ditau final state, as well as in the HL phase. For the case of gluon-fusion production in association with a $b\bar{b}$ pair (Fig. 8), we obtain slightly smaller values for $\sigma \cdot \text{BR}$, where, the point with the highest cross section is the same as in the previous process, with a mass of 132.27 GeV and with the signal rate of $\sigma \cdot \text{BR} = 0.0097 \text{ pb}$, which, at the

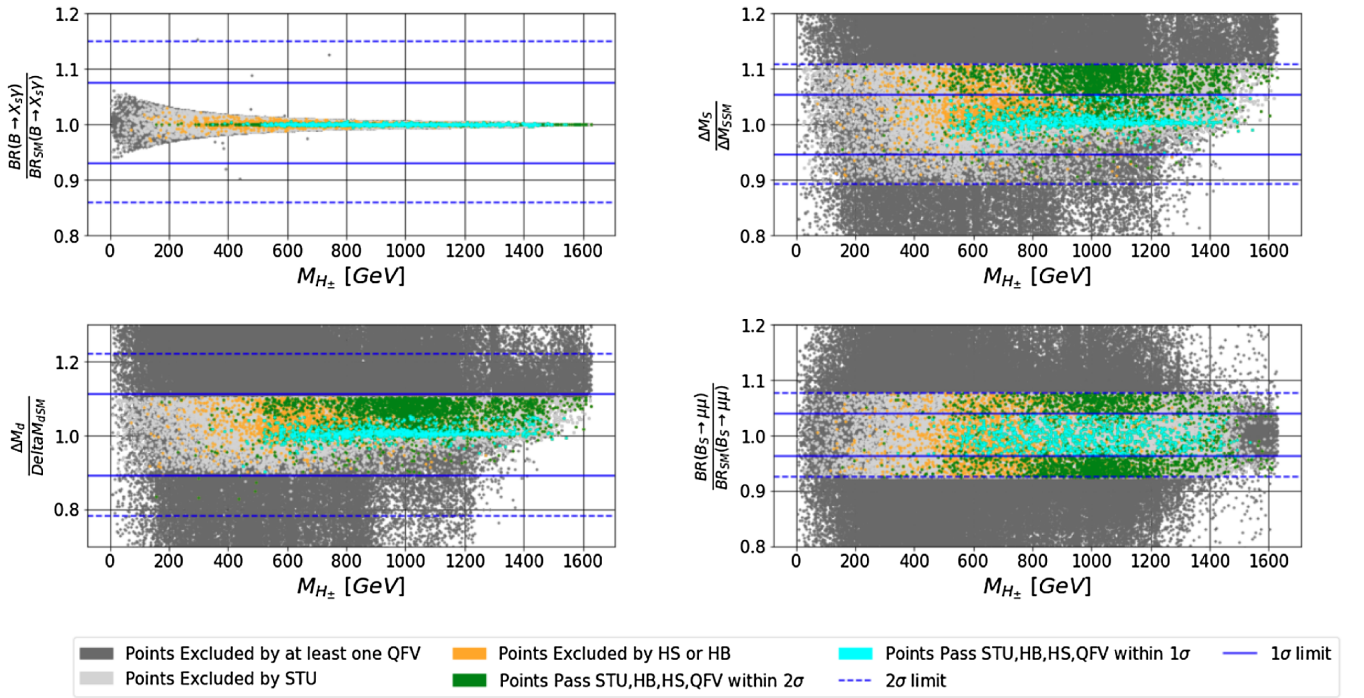


FIG. 7. Summary plots for the QFV variables. Dark gray points are excluded for at least one QFV observable in Table IV while light gray points do not pass the EW precision tests. Orange points are excluded either by HB or HS and green (cyan) points are compatible with EW and Higgs physics as well as all QFV constraints at a 2σ (1σ) level.

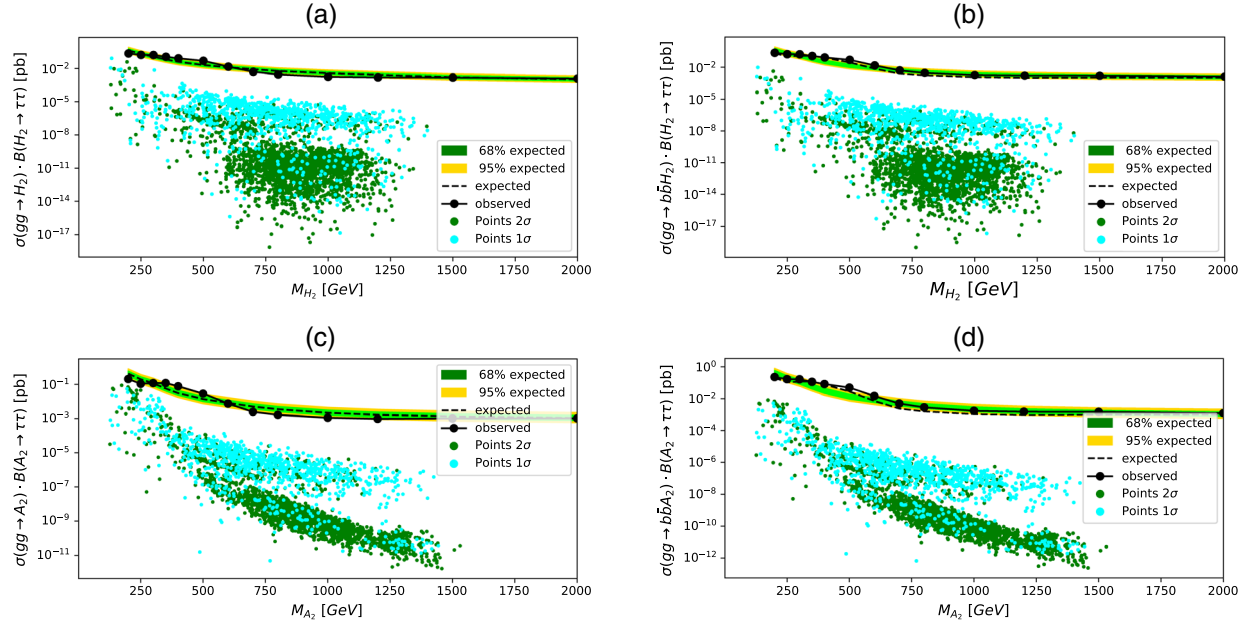


FIG. 8. The signal strength for production of a CP -even (top panels) and a CP -odd (bottom panels) scalar via the gluon-gluon fusion mechanism (a), (c) times its branching ratio to $\tau\bar{\tau}$, and (b), (d) with associated production of a $b\bar{b}$ -pair times its branching fraction to $\tau\bar{\tau}$, as a function of the lightest CP -even mass, M_{H_2} (top panels) and lightest pseudoscalar mass M_{A_2} (bottom panels). Green points satisfy QFV observables within 2 standard deviations, whereas blue ones pass QFV constraints at 1σ . Green and yellow error bands correspond to the limits set by the ATLAS experiment [43] including run-II data collected at $\sqrt{s} = 13$ TeV.

(run III) HL phase, corresponds to an expected number of events of around $N \sim (2910)29100$. As such, one can test this channel at both run-III and HL-LHC. A better picture is expected for the pseudoscalar production as one can see in the bottom panels of Fig. 8, where one can find cross sections 1 to 2 orders of magnitude larger when compared to the analogous H_2 productions and decay channels.

The small signal strengths found for the ditau final states are, to a large extent, a result of the small branching fractions generically observed for $H_2 \rightarrow \tau^+\tau^-$ decays. Indeed, as one can see in Table VI, for a selection of five benchmark points, the values of $\text{BR}(H_2 \rightarrow \tau^+\tau^-)$ are always subdominant, with the exception of benchmarks with sizable cross sections.

TABLE VI. A selection of five benchmark points (BP) that respect all QFV, electroweak, Higgs, and theoretical constraints. All masses are given in GeV and cross sections in pb. These correspond to H_2 early discovery scenarios that maximize the signal strength to dibosons (BP1,BP2), and to later H_2 and A_2 discovery cases that maximize the ditau channel (BP4) and again (BP2), respectively. The (BP3) represents the second lightest M_{H_2} scenario while (BP5) was chosen to represent scenarios with heavier H_2 which preferably decay to $A_2 Z^0$. Ditau final states are showcased while in the last column we provide the dominant decay mode with the respective branching ratio.

ϕ	ID	Mass (GeV)	$\text{BR}(\phi \rightarrow \tau^+\tau^-)$	$\sigma(gg \rightarrow \phi) \cdot \text{BR}$ (pb)	$\sigma(gg \rightarrow \bar{b}b\phi) \cdot \text{BR}$ (pb)	Maximum BR
H_2	BP1	160.21	4.99×10^{-3}	0.007354	8.01×10^{-4}	$\text{BR}(W^+W^*) = 0.881$
	BP2	347.99	6.65×10^{-7}	3.25×10^{-8}	3.67×10^{-9}	$\text{BR}(H_1H_1) = 0.611$
	BP3	129.26	0.0127	3.59×10^{-4}	4.3×10^{-5}	$\text{BR}(W^+W^*) = 0.377$
	BP4	132.27	0.0357	0.0830	0.00967	$\text{BR}(b\bar{b}) = 0.590$
	BP5	668.49	6.14×10^{-6}	7.42×10^{-8}	1.01×10^{-8}	$\text{BR}(A_2 Z^0) = 0.75$
A_2	BP1	194.99	0.0336	0.0546	0.00532	$\text{BR}(b\bar{b}) = 0.553$
	BP2	173.55	0.0264	0.0874	0.008249	$\text{BR}(b\bar{b}) = 0.432$
	BP3	1077.21	2.65×10^{-5}	1.0×10^{-6}	1.62×10^{-7}	$\text{BR}(\bar{t}t) = 0.711$
	BP4	937.61	3.49×10^{-5}	6.36×10^{-9}	8.66×10^{-10}	$\text{BR}(\bar{t}t) = 0.918$
	BP5	126.74	2.48×10^{-3}	3.2×10^{-5}	3.0×10^{-6}	$\text{BR}(c\bar{c}) = 0.922$

TABLE VII. A selection of five benchmark points (BP) that respect all QFV, electroweak, Higgs, and theoretical constraints. All masses are given in GeV and cross sections in pb. The benchmark points are the same as in Table VI. Diboson final states are showcased while in the last column we provide the dominant decay mode with the respective branching ratio.

ϕ	ID	Mass (GeV)	$\text{BR}(\phi \rightarrow W^+W^-)$	$\text{BR}(\phi \rightarrow Z^0Z^0)$	$\sigma(gg \rightarrow \phi \rightarrow W^+W^-)$ (pb)	$\sigma(gg \rightarrow \phi \rightarrow Z^0Z^0)$ (pb)	Maximum BR
H_2	BP1	160.21	0.881	0.0210	1.0032	0.00054	$\text{BR}(W^+W^*) = 0.881$
	BP2	347.99	0.129	0.0589	0.00722	0.003319	$\text{BR}(H_1H_1) = 0.611$
	BP3	129.26	0.377	0.0449	3.0×10^{-6}	1.0×10^{-6}	$\text{BR}(W^+W^*) = 0.377$
	BP4	132.27	0.239	0.0299	0.00366	0.001426	$\text{BR}(b\bar{b}) = 0.590$
	BP5	668.49	0.416	0.203	0.00506	0.00244	$\text{BR}(A_2Z^0) = 0.75$
H_3	BP1	929.20	0.124	0.0616	0.00341	0.00167	$\text{BR}(H_1H_1) = 0.456$
	BP2	823.89	0.0922	0.0455	1.36×10^{-4}	6.7×10^{-5}	$\text{BR}(A_2A_2) = 0.228$
	BP3	1093.01	0.166	0.0824	0.002964	0.001468	$\text{BR}(H_1H_1) = 0.531$
	BP4	1156.49	0.0598	0.0297	0.000192	9.4×10^{-5}	$\text{BR}(t\bar{t}) = 0.617$
	BP5	754.64	0.0517	0.0254	8.4×10^{-4}	4.1×10^{-4}	$\text{BR}(t\bar{t}) = 0.591$

Similar conclusions are obtained for the pseudoscalar case as one can see in the bottom plots of Fig. 8 and in the lower half of Table VI. However, as mentioned above, A_2 production cross sections with subsequent decay into taus tend to be greater when compared to H_2 , with the largest value encountered reaching 0.087 pb for a pseudoscalar with mass 174 GeV.

The benchmark points BP4 and BP2 in Tables VI and VII summarize the discussion of the previous two paragraphs, which were selected as the ones offering the larger H_2 and A_2 production and decay cross sections, respectively. For various displayed benchmarks, while for the H_2 field one finds multiple final states worth exploring, for the A_2 we note that quark decays are typically preferred. For the pseudoscalar case, we highlight benchmarks BP4 and BP5, which result in a final state with two tops and two charm quarks, respectively. In the later case, it would result in a final state with two light jets in the detector, whereas for the former case, one would expect at least two b -jets plus two W bosons in the final state, following the decay of the top quarks.

Besides some points in the low-mass region, the small branching ratios are generically obtained for the scalar and pseudoscalar decays into a pair of taus, and as such one might wonder what then the dominant channels are. The answer is in part given in the last column of Table VI, where we have found that H_2 mostly decays to $b\bar{b}$ and WW pairs, as well as into A_2Z^0 and two Higgs bosons, H_1H_1 . The first would result in a signature with two b -jets at the LHC while the second either in a pair of jets or a pair of leptons or even a jet and a lepton, together with missing energy. Note that the $H_2 \rightarrow A_2Z^0$ decay channel results in an interesting signature with at least four jets or two jets + two leptons, where we assume that the A_2 scalar

mostly decays into c -jets, according to the discussion above. A more detailed analysis of this channel deserves special attention and its collider phenomenology is being the subject of a separate study currently in preparation. Notice that the $H_2 \rightarrow A_2Z^0$ decay channel becomes increasingly important for heavier CP -even scalars as opposed to lighter H_2 scenarios where the pure SM decays dominate. One must also mention that H_2 can decay in a pair of Higgs bosons. Such a possibility is rather interesting as it can lead to a final state with $4b$ -jets (via the chain $pp \rightarrow H_2 \rightarrow H_1H_1 \rightarrow b\bar{b}b\bar{b}$). Indeed, both ATLAS and CMS have searched for Higgs boson pairs in the four b -jets final state [46–48].

In Table VII one can also see that, even when not the dominant contributions, the decay of CP -even scalars into diboson final states offer larger branching ratios than those of the tau channel. Recall that, in this article, we do not assume an exact Higgs alignment limit. Instead, we allow for small deviations from it, while still guaranteeing a SM-like Higgs candidate to have its mass and interactions within experimental bounds. In turn, the new CP -even scalars can couple to both Z^0 and W^\pm bosons and constraints arising from LHC direct searches, considering the $\phi \rightarrow W^+W^-$ and $\phi \rightarrow Z^0Z^0$ channels, with $\phi = H_2, H_3$, become relevant to our analysis. The results are summarized in the plots of Fig. 9, for both the H_2 (left panels) and H_3 (right panels). As expected, all points remain below the experimental bounds but with larger signal strengths in comparison with the ditau channel. In fact, most of points shown on panels a) and c) can be at the reach of the LHC run-III or its HL phase. In particular, we have found that for the diboson channel with Z^0Z^0 , a big portion of the allowed points comes close to the lower bound set by experiment, with the largest allowed cross sections being

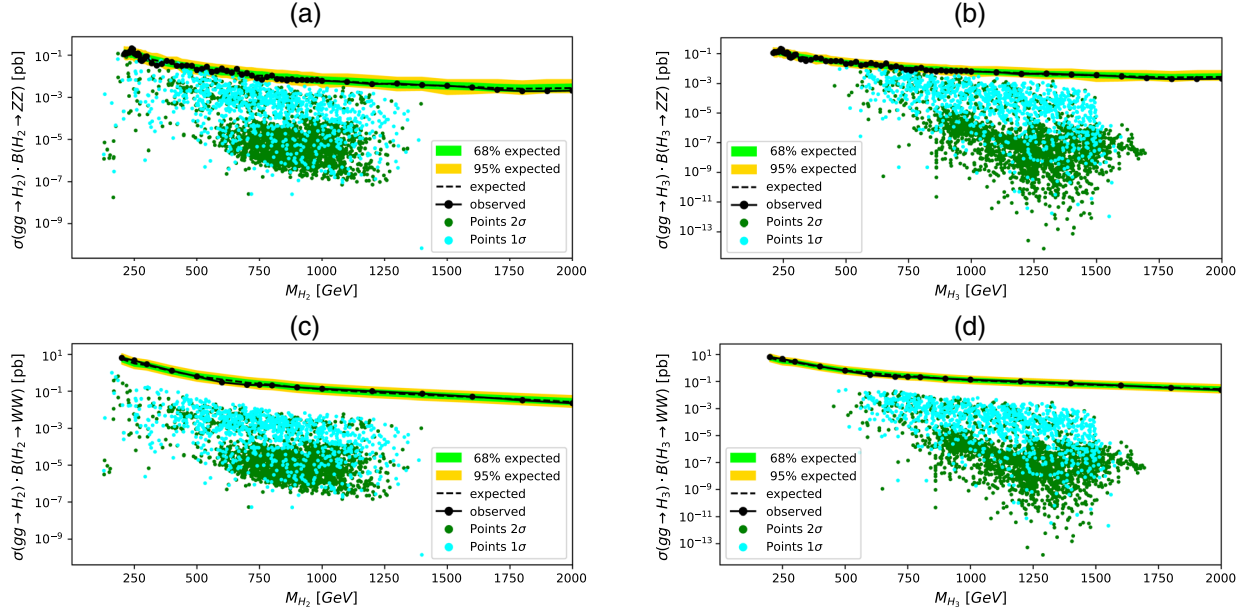


FIG. 9. The signal strength for production of a CP -even scalars via the gluon-gluon fusion mechanism (a), (b) times its branching ratio to ZZ , and (c), (d) times its branching fraction to WW , as a function of the lightest CP -even mass, M_{H_2} (left panels) and heaviest CP -even mass M_{H_3} (right panels). The color code is the same as in Fig. 8 and the exclusion bounds were taken from [40,44].

of the order of $\mathcal{O}(10^{-1})$ and $\mathcal{O}(10^{-3})$ pb. Therefore, it is possible the upcoming measurements would be capable of probing the allowed parameter space of the model. Note that for these two cases, the decay into a pair of W bosons is indeed the dominant channel. These points are very close to the ATLAS limit marking them as interesting benchmarks for an early probing, already with run-III data. It is also worth mentioning that, by virtue of a sizeable branching ratio to a W boson pair, the signal strength for the heavy CP -even state H_3 is comparable to those obtained for the lighter H_2 state. Finally, let us comment that, for the case of pseudoscalars, only the tau channel is considered given that tree-level couplings of A_2 to vector bosons are forbidden. Radiative effects where such processes can be induced are beyond the scope of our discussion in this article.

VII. CONCLUSIONS

We have discussed anomaly free implementations of a NTHDM-BGL model containing three generations of right-handed neutrinos, imbuing masses to the active left-handed neutrinos via a Type-I seesaw mechanism. We have specialized our numerical analysis on a version denoted as ν BGL-I where flavor violation processes are expected only on the down-type quarks sector. We have constrained the allowed parameter space of the model upon imposing electroweak precision, Higgs, and flavor physics constraints and scouted the parameter space in a search for phenomenologically valid regions. We have successfully

assessed the viability of the low mass region and found that even for a number of scenarios with new scalars at, or at least very close to the EW scale, the ν BGL-I model remains unconstrained. On the other hand, the majority of the excluded scenarios met their fate due to a combined effect of the ΔM_s and $\text{BR}(B_s \rightarrow \mu\mu)$ QFV observables, which have eliminated approximately 90.61% of the sampled points.

For the points that have survived all constraints we have confronted our results with existing direct searches at the LHC. We have found that new CP -even scalars are largely favoring final states with a pair of W bosons for masses not far from the EW scale. However, as their mass grows, the decay channel $H_2 \rightarrow A_2 Z^0$ becomes dominant, thus a preferable option for further searches at the LHC run-III or HL phases. Last but not least, while our results confirm that the ditau channel is well suited for pseudoscalar searches, their decay branching ratios to a pair of quarks is in general largely dominant.

ACKNOWLEDGMENTS

Useful discussions and helpful correspondence with Mark Goodsell are gratefully acknowledged. J. G., F. F. F., A. P. M., and V. V. are supported by the Center for Research and Development in Mathematics and Applications (CIDMA) through the Portuguese Foundation for Science and Technology (FCT—Fundação para a Ciência e a Tecnologia), references UIDB/04106/2020 and UIDP/04106/2020. A. P. M., F. F. F., J. G., and V. V. are supported

by the project PTDC/FIS-PAR/31000/2017. A. P. M. is also supported by national funds (OE), through FCT, I. P., in the scope of the framework contract foreseen in the numbers 4, 5, and 6 of the article 23, of the Decree-Law 57/2016, of August 29, changed by Law 57/2017, of July 19. J.G is also directly funded by FCT through a doctoral program grant with the reference 2021.04527.BD. R. P. is supported in part by the Swedish Research Council grant, contract number 2016-05996, as well as by the European Research Council (ERC) under the European Union's Horizon 2020 research and innovation programme (grant agreement No. 668679). P. F. is supported by CFTC-UL under FCT contracts UIDB/00618/2020, UIDP/00618/2020, and by the projects CERN/FIS-PAR/0002/2017 and CERN/FIS-PAR/0014/2019.

APPENDIX A: ANOMALY CONDITIONS AND CHARGE ASSIGNMENT

The anomaly cancellation conditions independent of the neutrino flavor charges read as

$$\begin{aligned}
 a_1 &= a_2 + \frac{(M_{A_2}^2 - M_{A_3}^2) \sin(2\gamma_1)}{\sqrt{2}v}, \\
 \mu_3^2 &= \frac{M_{A_3}^2 \sin^2(\gamma_1) (\cot(\gamma_1) v_S - v \sin(\beta) \cos(\beta)) - M_{A_2}^2 \cos^2(\gamma_1) (\tan(\gamma_1) v_S + v \sin(\beta) \cos(\beta))}{v} - \sqrt{2} a_2 v_S, \\
 \mu_b^2 &= -\frac{1}{2v_S} (\sqrt{2} a_2 v^2 \sin(\beta) \cos(\beta) + M_{A_3}^2 \cos(\gamma_1) (\cos(\gamma_1) v_S - v \sin(\beta) \cos(\beta) \sin(\gamma_1)) \\
 &\quad + M_{A_2}^2 \sin(\gamma_1) (\sin(\gamma_1) v_S + v \sin(\beta) \cos(\beta) \cos(\gamma_1))), \\
 \lambda_1 &= \frac{1}{4v^2} (\sec^2(\beta) (-\sin^2(\beta) ((M_{A_2}^2 - M_{A_3}^2) \cos(2\gamma_1) + M_{A_2}^2 + M_{A_3}^2) + \sin(\alpha_2) \sin(2\alpha_3) (M_{H_2}^2 - M_{H_3}^2) \sin(2(\alpha_1 - \beta)) \\
 &\quad + 2\cos^2(\beta - \alpha_1) (\cos^2(\alpha_2) M_{H_1}^2 + \sin^2(\alpha_2) (\sin^2(\alpha_3) M_{H_2}^2 + \cos^2(\alpha_3) M_{H_3}^2)) \\
 &\quad + 2\sin^2(\beta - \alpha_1) (\sin^2(\alpha_3) M_{H_3}^2 + \cos^2(\alpha_3) M_{H_2}^2)), \\
 \lambda_2 &= \frac{1}{4v^2} (\csc^2(\beta) (-2\cos^2(\beta) (M_{A_3}^2 \sin^2(\gamma_1) + M_{A_2}^2 \cos^2(\gamma_1)) + \sin(\alpha_2) \sin(2\alpha_3) (M_{H_3}^2 - M_{H_2}^2) \sin(2(\alpha_1 - \beta)) \\
 &\quad + 2\cos^2(\alpha_2) M_{H_1}^2 \sin^2(\beta - \alpha_1) + 2\sin^2(\alpha_2) \sin^2(\beta - \alpha_1) (\sin^2(\alpha_3) M_{H_2}^2 + \cos^2(\alpha_3) M_{H_3}^2) \\
 &\quad + 2\cos^2(\beta - \alpha_1) (\sin^2(\alpha_3) M_{H_3}^2 + \cos^2(\alpha_3) M_{H_2}^2)), \\
 \lambda_3 &= \frac{1}{2v^2} (\csc(\beta) \sec(\beta) (2\sqrt{2}(a_1 + a_2) v_S - \sin(2(\alpha_1 - \beta)) (\cos^2(\alpha_2) M_{H_1}^2 + \cos^2(\alpha_3) (\sin^2(\alpha_2) M_{H_3}^2 - M_{H_2}^2)) \\
 &\quad + \sin(\alpha_2) \sin(2\alpha_3) (M_{H_2}^2 - M_{H_3}^2) \cos(2(\alpha_1 - \beta)) + 4\mu_3^2) + 2M_{A_3}^2 \sin^2(\gamma_1) + 2M_{A_2}^2 \cos^2(\gamma_1) + 4M_{H^{\text{pm}}}^2 \\
 &\quad + \sin^2(\alpha_3) \csc(2\beta) \sin(2(\alpha_1 - \beta)) (\cos(2\alpha_2) M_{H_2}^2 - M_{H_2}^2 + 2M_{H_3}^2)), \\
 \lambda_4 &= -\frac{\csc(\beta) \sec(\beta) (\sqrt{2}(a_1 + a_2) v_S + \sin(2\beta) M_{H^\pm}^2 + 2\mu_3^2)}{v^2}, \\
 \lambda'_1 &= \frac{1}{2v_S^3} (v \sin(\beta) \cos(\beta) (\sqrt{2} a_2 v + (M_{A_2}^2 - M_{A_3}^2) \sin(\gamma_1) \cos(\gamma_1)) + \sin^2(\alpha_2) M_{H_1}^2 v_S \\
 &\quad + \cos^2(\alpha_2) v_S (\sin^2(\alpha_3) M_{H_2}^2 + \cos^2(\alpha_3) M_{H_3}^2)),
 \end{aligned}$$

$$\begin{aligned}
 A_{U(1)_Y U(1)_{Y'} U(1)_{Y''}} &\equiv \sum_{i=1}^3 (X_{q_i} + 3X_{l_i} - 8X_{u_i} - 2X_{d_i} - 6X_{e_i}) = 0, \\
 A_{U(1)_Y U(1)_{Y'} U(1)_{Y''}} &\equiv \sum_{i=1}^3 (X_{q_i}^2 - X_{l_i}^2 - 2X_{u_i}^2 + X_{d_i}^2 + X_{e_i}^2) = 0, \\
 A_{SU(2)_L SU(2)_{L'} U(1)_{Y'}} &\equiv \sum_{i=1}^3 (3X_{q_i} + X_{l_i}) = 0, \\
 A_{SU(3)_C SU(3)_{C'} U(1)_{Y'}} &\equiv \sum_{i=1}^3 (2X_{q_i} - X_{u_i} - X_{d_i}) = 0, \tag{A1}
 \end{aligned}$$

with the A_{XYZ} factor already defined in the main text below Eq. (3.13).

APPENDIX B: ANALYTICAL EQUATIONS FOR THE LAGRANGIAN PARAMETERS

$$\begin{aligned}\lambda'_2 &= -\frac{1}{vv_S}(\sec(\beta)(\sin(\beta)(\sqrt{2}a_2v + (M_{A_2}^2 - M_{A_3}^2)\sin(\gamma_1)\cos(\gamma_1)) + \cos(\alpha_2)(\sin(\alpha_2)\cos(\beta - \alpha_1)(\sin^2(\alpha_3)M_{H_2}^2 \\ &\quad + \cos^2(\alpha_3)M_{H_3}^2 - M_{H_1}^2) - \sin(\alpha_3)\cos(\alpha_3)(M_{H_2}^2 - M_{H_3}^2)\sin(\beta - \alpha_1))), \\ \lambda'_3 &= -\frac{1}{vv_S}(\csc(\beta)(\cos(\beta)(\sqrt{2}a_2v + (M_{A_2}^2 - M_{A_3}^2)\sin(\gamma_1)\cos(\gamma_1)) + \cos(\alpha_2)(\sin(\alpha_3)\cos(\alpha_3)(M_{H_2}^2 - M_{H_3}^2)\cos(\beta - \alpha_1) \\ &\quad - \sin(\alpha_2)\sin(\beta - \alpha_1)(-\sin^2(\alpha_3)M_{H_2}^2 - \cos^2(\alpha_3)M_{H_3}^2 + M_{H_1}^2))).\end{aligned}$$

For completeness, in the case of a model with a neutral singlet [that is, with a $U(1)'$ charge of zero], all a_1 , a_2 , a_3 , and a_4 would be simultaneously allowed, resulting in modified expressions for the parameters of the scalar potential apart from λ'_3 . These are

$$\begin{aligned}a_4 &= \frac{1}{2vv_S}((-M_{A_2}^2 + M_{A_3}^2)\sin 2\gamma_1 + \sqrt{2}v(a_1 - a_2) + 2vv_S a_3), \\ \mu_3^2 &= \frac{1}{4v}(-v(M_{A_2}^2 + M_{A_3}^2 + (M_{A_2}^2 - M_{A_3}^2)\cos 2\gamma_1 \sin 2\beta) + (M_{A_2}^2 - M_{A_3}^2)v_S \sin 2\gamma_1 + vv_S(-\sqrt{2}(3a_1 + a_2) - 4v_S a_3)), \\ \mu_b^2 &= \frac{1}{4v_S}(-(M_{A_2}^2 + M_{A_3}^2)v_S + (M_{A_2}^2 - M_{A_3}^2)(v_S \cos 2\gamma_1 + v \sin 2\beta \sin 2\gamma_1) + v^2 \cos \beta \sin \beta(-3\sqrt{2}a_1 + \sqrt{2}a_2 - 8v_S a_3)), \\ \lambda_1 &= -\frac{1}{2v^2}\left(\sec^2\beta\left(-M_{H_1}^2 \cos^2\alpha_2 \cos^2\delta + \frac{1}{2}(M_{A_2}^2 + M_{A_3}^2 + (M_{A_2}^2 - M_{A_3}^2)\cos 2\gamma_1)\right)\sin^2\beta\right. \\ &\quad \left.- M_{H_2}^2(\cos \delta \sin \alpha_2 \sin \alpha_3 + \cos \alpha_3 \sin \delta)^2 - M_{H_3}^2(\cos \alpha_3 \cos \delta \sin \alpha_2 - \sin \alpha_3 \sin \delta)^2\right), \\ \lambda_2 &= \frac{1}{2v^2}\csc^2\beta(M_{H_3}^2 \cos^2\delta \sin^2\alpha_3 - \cos^2\beta(M_{A_2}^2 \cos^2\gamma_1 + M_{A_3}^2 \sin^2\gamma_1) \\ &\quad + (M_{H_1}^2 \cos^2\alpha_2 + M_{H_2}^2 \sin^2\alpha_2 \sin^2\alpha_3)\sin^2\delta + \cos^2\alpha(M_{H_2}^2 \cos^2\delta + M_{H_3}^2 \sin^2\alpha_2 \sin^2\delta) \\ &\quad + (-M_{H_2} + M_{H_3}^2)\cos \alpha_3 \sin \alpha_2 \sin \alpha_3 \sin 2\delta), \\ \lambda_3 &= \frac{1}{8v^2}(-4(M_{A_2}^2 + M_{A_3}^2 - 4M_{H^\pm}^2) + 4(-M_{A_2}^2 + M_{A_3}^2)\cos 2\gamma_1 \\ &\quad + \csc \beta \sec \beta(4(M_{H_2}^2 - M_{H_3}^2)\cos 2\delta \sin \alpha_2 \sin 2\alpha_3 + (2(-2M_{H_1}^2 + M_{H_2}^2 + M_{H_3}^2)\cos^2\alpha_2 \\ &\quad - (M_{H_2}^2 - M_{H_3}^2)(-3 + \cos 2\alpha_2)\cos 2\alpha_3)\sin 2\delta)), \\ \lambda_4 &= \frac{1}{v^2}(M_{A_2}^2 + M_{A_3}^2 - 2M_{H^\pm}^2 + (M_{A_2}^2 - M_{A_3}^2)\cos 2\gamma_1), \\ \lambda'_1 &= \frac{1}{4v_S^3}(2v_S(M_{H_1}^2 \sin^2\alpha_2 + \cos^2\alpha_2(M_{H_3}^2 \cos^2\alpha_3 + M_{H_2}^2 \sin^2\alpha_3)) + \sqrt{2}v^2 \cos \beta \sin \beta(a_1 + a_2)), \\ \lambda'_2 &= \frac{1}{vv_S}(\cos \alpha_2 \sec \beta(\cos \delta \sin \alpha_2(M_{H_1}^2 - M_{H_3}^2 \cos^2\alpha_3 - M_{H_2}^2 \sin^2\alpha_3) \\ &\quad + (-M_{H_2}^2 + M_{H_3}^2)\cos \alpha_3 \sin \alpha_3 \sin \delta) + (M_{A_2}^2 - M_{A_3}^2)\cos \gamma_1 \sin \gamma_1 \tan \beta - v(\sqrt{2}a_1 + 2v_S a_3)\tan \beta),\end{aligned}$$

and where the minimization conditions only modify μ_S^2 and $\hat{\mu}$ as

$$\mu_S^2 = -\frac{\sqrt{2}v_1 v_2(a_1 + a_2) + v_S(v_1(2v_2(a_3 + a_4) + v_1\lambda'_2) + v_2^2\lambda'_3 + 2(v_S^2\lambda'_1 + \mu_b^2))}{2v_S}$$

and

$$\hat{\mu} = v_S[\sqrt{2}(a_1 + a_2) + v_S(a_3 + a_4)] + v_1 v_2(\lambda_3 + \lambda_4) + 2\mu_3^2.$$

- [1] G. Aad *et al.* (ATLAS Collaboration), *Phys. Lett. B* **716**, 1 (2012).
- [2] S. Chatrchyan *et al.* (CMS Collaboration), *Phys. Lett. B* **716**, 30 (2012).
- [3] T. D. Lee, *Phys. Rev. D* **8**, 1226 (1973).
- [4] A. E. Cárcamo Hernández, C. Espinoza, J. Carlos Gómez-Izquierdo, and M. Mondragón, [arXiv:2104.02730](https://arxiv.org/abs/2104.02730).
- [5] G. Arcadi, A. S. de Jesus, T. B. de Melo, F. S. Queiroz, and Y. S. Villamizar, *Nucl. Phys.* **B982**, 115882 (2022).
- [6] N. F. Bell, G. Busoni, and I. W. Sanderson, *J. Cosmol. Astropart. Phys.* **03** (2017) 015.
- [7] G. C. Dorsch, S. J. Huber, K. Mimasu, and J. M. No, *J. High Energy Phys.* **12** (2017) 086.
- [8] D. A. Camargo, M. D. Campos, T. B. de Melo, and F. S. Queiroz, *Phys. Lett. B* **795**, 319 (2019).
- [9] I. P. Ivanov, *Prog. Part. Nucl. Phys.* **95**, 160 (2017).
- [10] G. C. Branco, P. M. Ferreira, L. Lavoura, M. N. Rebelo, M. Sher, and J. P. Silva, *Phys. Rep.* **516**, 1 (2012).
- [11] B. Grzadkowski, O. M. Ogreid, and P. Osland, *J. High Energy Phys.* **01** (2014) 105.
- [12] R. Boto, T. V. Fernandes, H. E. Haber, J. C. Romão, and J. P. Silva, *Phys. Rev. D* **101**, 055023 (2020).
- [13] B. Grzadkowski, O. M. Ogreid, and P. Osland, *Phys. Rev. D* **94**, 115002 (2016).
- [14] D. Sokolowska, K. A. Kanishev, and M. Krawczyk, *Proc. Sci., CHARGED2008* (**2008**) 016 [[arXiv:0812.0296](https://arxiv.org/abs/0812.0296)].
- [15] A. Crivellin, A. Kokulu, and C. Greub, *Phys. Rev. D* **87**, 094031 (2013).
- [16] C. S. Kim, Y. W. Yoon, and X.-B. Yuan, *J. High Energy Phys.* **12** (2015) 038.
- [17] G. C. Branco, W. Grimus, and L. Lavoura, *Phys. Lett. B* **380**, 119 (1996).
- [18] A. Ordell, R. Pasechnik, and H. Serôdio, *Phys. Rev. D* **102**, 035016 (2020).
- [19] F. Nottensteiner, A. Ordell, R. Pasechnik, and H. Serôdio, *Phys. Rev. D* **100**, 115038 (2019).
- [20] M. D. Campos, D. Cogollo, M. Lindner, T. Melo, F. S. Queiroz, and W. Rodejohann, *J. High Energy Phys.* **08** (2017) 092.
- [21] G. Aad *et al.* (ATLAS Collaboration), *J. High Energy Phys.* **10** (2020) 061.
- [22] M. Aaboud *et al.* (ATLAS Collaboration), *J. High Energy Phys.* **10** (2018) 180.
- [23] G. Aad *et al.* (ATLAS Collaboration), *J. High Energy Phys.* **11** (2021) 209.
- [24] A. M. Sirunyan *et al.* (CMS Collaboration), *J. High Energy Phys.* **05** (2020) 033.
- [25] A. M. Sirunyan *et al.* (CMS Collaboration), *J. High Energy Phys.* **07** (2021) 208.
- [26] A. M. Sirunyan *et al.* (CMS Collaboration), *J. High Energy Phys.* **04** (2018) 073.
- [27] F. Staub, *Comput. Phys. Commun.* **185**, 1773 (2014).
- [28] W. Porod and F. Staub, *Comput. Phys. Commun.* **183**, 2458 (2012).
- [29] P. Bechtle, S. Heinemeyer, O. Stal, T. Stefaniak, and G. Weiglein, *Eur. Phys. J. C* **75**, 421 (2015).
- [30] P. Bechtle, S. Heinemeyer, O. Stål, T. Stefaniak, and G. Weiglein, *Eur. Phys. J. C* **74**, 2711 (2014).
- [31] D. M. Straub, [arXiv:1810.08132](https://arxiv.org/abs/1810.08132).
- [32] A. Ordell, Phenomenology in multiscale extensions of the Standard Model, Ph.D. thesis, Lund University, 2020.
- [33] F. J. Botella, G. C. Branco, M. Nebot, and M. N. Rebelo, *J. High Energy Phys.* **10** (2011) 037.
- [34] D. Das, P. M. Ferreira, A. P. Morais, I. Padilla-Gay, R. Pasechnik, and J. P. Rodrigues, *J. High Energy Phys.* **11** (2021) 079.
- [35] P. Zyla *et al.* (Particle Data Group), *Prog. Theor. Exp. Phys.* **2020**, 083C01 (2020).
- [36] M. Aaboud *et al.* (ATLAS Collaboration), *Phys. Rev. D* **98**, 052008 (2018).
- [37] V. Khachatryan *et al.* (CMS Collaboration), *Phys. Lett. B* **755**, 217 (2016).
- [38] V. Khachatryan *et al.* (CMS Collaboration), *Phys. Lett. B* **759**, 369 (2016).
- [39] G. Aad *et al.* (ATLAS Collaboration), *Phys. Rev. D* **102**, 032004 (2020).
- [40] G. Aad *et al.* (ATLAS Collaboration), *Eur. Phys. J. C* **81**, 332 (2021).
- [41] A. M. Sirunyan *et al.* (CMS Collaboration), *J. High Energy Phys.* **03** (2020) 055.
- [42] P. A. Zyla *et al.* (Particle Data Group), *Prog. Theor. Exp. Phys.* **2020**, 083C01 (2020).
- [43] G. Aad *et al.* (ATLAS Collaboration), *Phys. Rev. Lett.* **125**, 051801 (2020).
- [44] M. Aaboud *et al.* (ATLAS Collaboration), *Eur. Phys. J. C* **78**, 24 (2018).
- [45] J. Alwall, R. Frederix, S. Frixione, V. Hirschi, F. Maltoni, O. Mattelaer, H. S. Shao, T. Stelzer, P. Torrielli, and M. Zaro, *J. High Energy Phys.* **07** (2014) 079.
- [46] M. Aaboud *et al.* (ATLAS Collaboration), *J. High Energy Phys.* **01** (2019) 030.
- [47] A. M. Sirunyan *et al.* (CMS Collaboration), *J. High Energy Phys.* **01** (2019) 040.
- [48] A. M. Sirunyan *et al.* (CMS Collaboration), *Phys. Lett. B* **781**, 244 (2018).